THE UNIVERSITY OF READING

Department of Meteorology

Radar observations of mixing within frontal zones

Danny Chapman

A thesis submitted for the degree of Doctor of Philosophy

September 1998

Abstract

This thesis describes how the 3 GHz Doppler radar at Chilbolton has been used to observe Kelvin-Helmholtz billows and their environment. The observations have been used to understand the structure and location of large-amplitude billows within a warm frontal zone, and to estimate their impact on the environmental flow. The main results and conclusions include the following:

- In order to confidently identify the presence or absence of billows using Doppler radar, vertical cross-sections of the vertical derivative of the Doppler velocity should be viewed as the vertical wind shear within KH billows has an easily detectable characteristic braided signature. Results are presented making use of this ability to identify regions containing KH billows.
- A detailed analysis is presented of large-amplitude billows within a warm frontal zone, including calculations of the 3D airflow through the billows and observations of their structure and evolution. A new method of calculating momentum fluxes is described. Rough estimates of momentum flux profiles using this method suggest that the billows were responsible for a considerable change in the mean wind profile over their length.
- The larger-scale structure of the front has been analysed using the Meteorological Office Unified Model, and it is shown how the combination of the flow and thermodynamic structure determined properties of the billows that were observed. This analysis leads to the concept of Potential Shearing Instability, a mechanism for suddenly generating very low Richardson numbers on large spatial scales.

The thesis as a whole shows that Kelvin-Helmholtz billows may occur quite frequently in the free atmosphere, and that the effect on their environment can be significant. Their existence and properties also have implications for air traffic safety, atmospheric chemistry and pollution dispersion. Their effects in the free atmosphere are, however, neglected by some numerical weather prediction models; this may be a serious ommission.

Acknowledgements

I would like to thank Anthony Illingworth and Keith Browning, my supervisors, for taking me on and letting me enjoy three years here at the Meteorology department in Reading. Keith and I have had many (often rather long!) discussions, which, and this is the important point, I have enjoyed. I am very grateful to him for helping me develop my ability to think for myself, and for spending so much time reading everything that I've written. I also appreciate the comments and suggestions of Mike Pedder and Stephen Belcher.

Thanks go to everyone at Chilbolton and RAL who have been very helpful, and have supplied me with more data than I can deal with. I would not have been able to look at any of it without a number of Mark Blackman's programs, so I appreciate him letting me use them and also his help when he was here in the department. Thanks also to Peter Panagi for providing the model data, helping me use it and generally giving me useful advice.

The Meteorology Department here at Reading University is a very pleasant place to do a PhD. Thanks to all who have made my time here an enjoyable experience - especially to Robin for his frequent help and top computing tips, Hannah for generously letting me win at tetris, Andy for our occasional conversations concerning rats and marital bliss and John for aiding and abetting me in my attempt to waste time on an unprecedented scale (and on the croquet lawn too).

Most of all I'd like to thank my family for looking after me - Anna, Miss Murr, Miss Rowl, Mr Prowl, Mouse, Sherlock, Arthur, Moriarty and, last (as ever!) but certainly not least, Miss Mould.

Contents

CHAPTER 1

Introduction

1.1 Introduction and aims

This thesis describes Doppler radar observations of dynamical structures associated with precipitating frontal zones in the atmosphere. In particular, the ability of the radar to detect regions containing Kelvin-Helmholtz (KH) billows and to resolve air flow through them is used to understand their occurrence, structure and effect on the atmosphere. Although the onset, structure and evolution of KH billows has been established in "ideal" flows using theoretical and laboratory models, observations are necessary because it is not obvious *a priori* how common billows are in the atmosphere, on what spatial scales they occur, and what effect they have on the background state. This thesis shows that:

- Regions containing or *not* containing billows within regions of precipitation may be confidently identified using radar, even if the velocity perturbations are small, so long as the scale of the billows is resolvable by the radar.
- Billows occur quite frequently within frontal zones, and often occur over depths comparable with the depth of the frontal zone itself.
- By making observations on a wide range of scales, a process has been identified (potential shearing instability) which may cause the sudden onset of very low Richardson numbers, and thus very vigourous overturning by KH billows if sufficient vertical shear is also present. This process may occur in situations where there is lifting of an initially just unsaturated statically stable shear layer.
- High resolution radar measurements of the air flow within billows allows momentum flux

profiles to be calculated, and thus estimates made of the effect of billows on the background flow.

- Some numerical weather prediction (NWP) models, such as the Meteorological Office Unified Model (UM), neglect mixing by KH billows in the free atmosphere (i.e. above the boundary layer) and this may be an serious omission. In addition, the frequency and vigour of the mixing shown in the cases described in this thesis is relevant for understanding the vertical transport of pollutants and chemical species in the atmosphere, particularly in the vicinity of fronts.

Since this thesis is based mostly on observations made using Doppler radar, the next section will describe the principles of the type of radar used here. The remainder of this chapter will then describe some of the relevant results of analytical, numerical and laboratory models and experiments related to KH instability and billows, as in order to fully understand observations of dynamical processes they must be related to results obtained from idealised experiments in which the dependence of the process on background parameters describing the environmental conditions can be determined. There have also been a substantial number of observational studies of KH billows in the atmosphere, which are discussed here because these also help to put the observations described in later chapters into context.

1.2 Principles of Radar

The radar data (not including the UK FRONTIERS network data) used in this thesis all come from the 3 GHz multi-parameter radar (Goddard *et al.* 1994) at Chilbolton (51.15°N, 1.44°W). The principles behind such a radar are fairly straightforward. A transmitter unit produces a 3 GHz wave, which is pulse modulated with a frequency of 610 Hz (the pulse repetition frequency, PRF). This signal is transmitted in a narrow beam by a parabolic antenna dish. Objects in the path of the beam backscatter some fraction of the wave, producing an echo which may then, after being focussed by the dish, be detected by a receiver. The 3 GHz dish used at Chilbolton is sufficiently large (25 m) compared to the wavelength of the signal (10 cm) that the beam has a small angular spread, 75% of the power being contained within a cone of angular width 0.25°. The time interval between transmission and detection of the signal is directly proportional to the range of the target. The returned signal is thus divided up into range gates, each 75 m long, which are then averaged over in groups of 4 to give a gate length of 300 m. A selection of 300 range gates are processed and recorded, allowing data to be obtained out to 90 km beyond the minimum range, which is itself variable. The maximum range is 160 km, though clearly the angular resolution becomes a problem at such large ranges. Other problems, such as refraction of the beam by vertical refractive index gradients, and earth curvature, may also be important at large ranges.

1.2.1 Reflectivity and polarisation measurements

In general, the echo from a target volume will be generated by incoherent scattering from many small targets, normally water droplets or ice crystals/snow. Some scattering will also occur from insects and refractive index inhomogeneities, so useful data may be obtained (with quite severe limitations) even in the clear air. The properties of the returned signal can be used to obtain a number of useful parameters which depend on the targets and their environment. The simplest of these is the backscattered power integrated over the target volume, which gives the reflectivity factor, Z. If the targets are small spherical water droplets which Rayleigh scatter then the power returned by each scatterer is proportional to D^6 where D is the droplet diameter. The radar reflectivity factor, measured in units of mm^6 m^{-3}, is given by

$$Z = \sum_{unitvol} D^6$$

and must be obtained over a long enough period to give a statistically representative sample of the droplets in the target volume. 128 pulses are normally used to obtain this sample.

If the droplets conform to a drop-size distribution of the form $N_D = N_0 e^{-\Delta D}$ where Δ is a function of the rain-rate (obtained from observations) then Z(mm^6 m^{-3}) may be estimated as being directly proportional to $R^{1.5}$, where R is the rain rate in mm hr^{-1} (e.g. Joss and Waldvogel 1970). The constant of proportionality varies considerably from around 140 for drizzle to 500 for heavy rain in thunderstorms, so on its own this relation is of limited use. It is, however, used as the basis for the rain-rate estimates produced as part of FRONTIERS and NIMROD, a network of radars which scan in PPI modes (see below) producing a composite for the UK on a 5km grid every 15 minutes.

The reflectivity is normally quoted in log units so Z(dBZ)$= 10\log_{10}(Z/Z_r)$ where $Z_r = 1\text{mm}^6\ \text{m}^{-3}$. Thus rain rates of 100 mm hr^{-1} in a heavy thunderstorm correspond to a reflectivity of around 60 dBZ. Reflectivities of less than around 10 dBZ correspond to light drizzle.

The radar is capable of both transmitting and detecting signals which are vertically or horizontally polarised (referring to the electric field). The plane of polarisation alternates between pulses. The reflectivities used in this thesis refer to the reflectivity derived from the horizontally polarised component of the return from the horizontally polarised outgoing signal, i.e. Z_H.

The (log) ratio of the horizontally and vertically polarised reflectivities gives the differential reflectivity, so $Z_{dr} = 10\log_{10}(Z_H/Z_V)$, which may be used to estimate the axial ratio of droplets. As a raindrop falls, its axial ratio is determined by its size and fall-speed as a result of deformation due to air resistance, so Z_{dr} may be used to estimate raindrop size. This may then be used to refine rainfall estimates made using Z_H alone, as it constrains the drop size distribution.

Another parameter measured by the radar is the linear depolarisation ratio, $L_{dr} = 10\log_{10}(Z_{H,V}/Z_H)$ where $Z_{H,V}$ is the signal received with a horizontal polarisation from a vertically polarised transmission. Again, this may be used to make inferences about droplet properties. However, these two parameters (Z_{dr} and L_{dr}) have mainly been used in this thesis to delineate the bright band, where precipitation melts forming a layer of enhanced reflectivity as it falls through the 0°C level.

1.2.2 Doppler measurements

The main interest, for the purposes of this thesis, is in the Doppler measurements made by the radar. The droplets in the target volume will move relative to the radar as a result of falling at a speed close to their terminal velocity, and in addition they will be advected by the wind field (Fig. 1.1). The radial component of this velocity, which is called the Doppler velocity, V_d, may

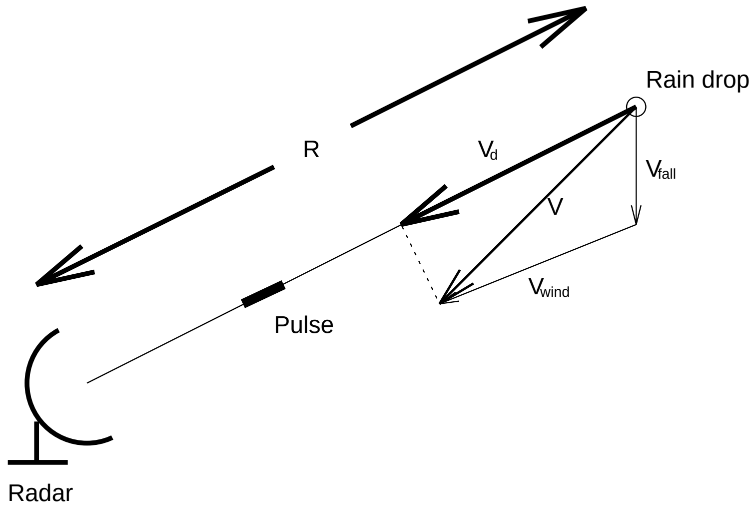

Figure 1.1: Schematic diagram showing how the different velocity contributions affect the Doppler velocity. V_{fall} represents the air-relative droplet fall velocity. V_{wind} represents the wind velocity. V represents the radar-relative droplet velocity. V_d is the Doppler velocity, i.e. the component of V along the radar beam. The vertical velocity components will generally be much smaller relative to the horizontal components than shown here. The target volume (containing many droplets) is at a distance R from the radar, so the echo is detected at a time $2R/c$ after the pulse is transmitted, where c is the speed of light.

be detected as a Doppler frequency shift in the returned signal, given by $\Delta f = 2V_d/\lambda$ where λ is the radar wavelength (10 cm). In practice this is done using an auto-covariance method using phase measurements of the outgoing and returning signals to give an estimate of the mean radial velocity of the scatterers, accurate to around 0.1 m s^{-1}. The ability to unambiguously detect phase measurements only between $-\pi$ and $+\pi$ means that the Doppler velocity may be "folded" so that it is always within the range -15 to +15 m s^{-1}. Normally data may be unfolded unambiguously by hand, although it is not possible to construct an infallible algorithm for doing this.

Although only the mean Doppler velocity is recorded at present from the Chilbolton radar, in studies using other radars (e.g. James and Browning 1981) the entire Doppler spectrum has been recorded. The problem with this is that very large amounts of data have to be processed and recorded in real-time as observations are being made. A compromise would be to record the spectral width of the main peak in the Doppler spectrum, as this gives some indication of the air motions occuring on scales below the radar resolution (i.e. turbulence). Although this still requires real-time analysis, it does not increase greatly the amount of data that must be recorded.

The spectral width, once corrected for contributions such as those due to the wind shear and finite beam width, may be used to provide estimates of the turbulent dissipation rate and the turbulent eddy diffusivity. However, the breakdown of certain assumptions, such as that the turbulent structure is homogeneous and isotropic throughout the scanning volume, may make such calculations susceptible to considerable errors. Further details and problems associated with this technique are given Doviak and Zrnic (1984).

1.2.3 Scanning modes and basic radar data analysis

There are a number of basic scanning modes used to collect data. In a PPI (Plan Position Indicator) the radar beam is scanned in azimuth at a fixed elevation. For low elevations, this effectively gives a plan view, although the change in height of the beam with range can be misleading. In an RHI (Range Height Indicator) the beam is scanned in elevation at a fixed azimuth. This gives a vertical cross-section. Normally the dish moves at its maximum rate of 1° sec^{-1}. This means that it takes six minutes to complete a 360° PPI, during which time the feature of interest may have changed significantly. The beam may also be held at a fixed azimuth and elevation, although such scans were not used in the analyses presented in this thesis. A CAPPI (Constant Altitude Plan Position Indicator) giving a horizontal cross-section may be reconstructed from a number of PPIs or RHIs, made at closely spaced elevations or azimuths, respectively.

All the quantitative analysis of data in this thesis has been made at elevations angles lower than around 10°. At this elevation angle, the ground-relative droplet fall speed, taking a rather extreme value of 5 m s^{-1}, contributes up to 1 m s^{-1} to the Doppler velocity. For the vast majority of the data, this vertical contribution is much smaller than this. The main contribution to the Doppler velocity comes from the radial component of the horizontal wind field. This is underestimated by only around 2% at an elevation of 10°. Consequently, the Doppler velocity has been taken as giving the radial component of the horizontal wind field, both at elevations less than 10° where this approximation is valid, and also in the semi-quantitative analyses of data at elevations up to 25°, where the horizontal wind component still dominates.

There are two principal sources of noise in the Doppler data resulting from ground clutter and a lack of suitable targets. Ground clutter occurs when either the main beam or side lobes produce returns from the ground, in the latter case giving erroneous values up to a few kilometers above the ground. In regions of very low reflectivity where there is no precipitation, the phase measurements, and therefore the Doppler velocities, are random. It is necessary to remove this noise before any integrations are done on the data. One way of doing this is to mask the Doppler field with the reflectivity, removing Doppler data wherever the reflectivity is below a certain threshold. However, for much of the data used here, reflectivity data below 0 dBZ were not recorded, even though the Doppler data may still be valid when the reflectivity is below this value. In addition, such a method will not remove the signals generated by the intersection with the ground of side-lobes from the main radar beam. Instead, the following method has been used, which depends only upon the Doppler field itself:

- For each value in the array of Doppler data, the variance of all the surrounding points is calculated relative to that value.
- Data where the variance is greater than a threshold (say 5 for RHIs, 6 for PPIs) are removed.
- Data points surrounded by more than, say, 4 data-free points are removed (to prevent spurious data in regions containing noise)
- Data-free points surrounded by more than, say, 4 data points are replaced (to prevent "holes" occurring in valid data due to locally large shears).

One advantage of masking the Doppler data in this way is that it allows the data to be unfolded automatically, using a simple (but fallible) algorithm. It also reveals small regions of valid data which could easily be missed when they occur within large regions of noise.

1.2.4 Clear air observations

The radar at Chilbolton is also capable of making measurements in the clear air. Although such measurements are not used in this thesis, clear-air observations of billows were made frequently using other radars, especially during the 1970's. The main source of reflectivity for clear-air radar observations comes from Bragg scatter due to refractive index inhomogeneities on the scale of half the wavelength. However, the reflectivity is very small, so the radar needs to be powerful and sensitive, and measurements can only be made within a fairly short range of the radar. One way of improving the sensitivity is to average over a greater number of pulses, but this leads to either a reduced effective angular resolution or a slower scan rate.

1.3 The dynamics of Kelvin-Helmholtz instability and billows

1.3.1 Onset of instability: idealised models

KH billows of finite amplitude occur as a result of the instability of a vortex sheet or shear layer which is statically stable. They have been studied using analytical and modelling methods as well as using laboratory experiments and observations in the atmosphere and ocean. Although these studies have resulted in some aspects of their structure and evolution becoming well understood, other aspects especially those involving their breakdown in real flows are still much less certain.

The basic mechanism behind the instability is intuitively quite straightforward. Batchelor (1967) and Drazin and Reid (1981) considered a velocity discontinuity in a two-dimensional flow, so that there is a vortex sheet as indicated in Fig. 1.2. For each point (through which a vortex line passes) in the sheet, the vorticity implies a clockwise circulation around the point, although if the sheet is flat the vertical components of these induced flows will all cancel out. Also, vortex lines are carried with the fluid flow, so that the vorticity is conserved following the flow.

Now, if there is a sinusoidal disturbance to the height of the sheet, the evolution of this disturbance may be deduced. There are essentially four types of location on the sheet: A, B, C and D, at the peak, minimum slope, trough and maximum slope locations respectively. The flow at point A is induced by the vorticity at all other points in the vortex sheet, all of which are either below or at the same height as A. Thus, the induced flow at A will be to the right, which will in turn advect vortex lines at A to the right. Similarly, vortex lines at C will be advected to the left, resulting in an increased concentration of vorticity at B, and a decreased concentration at D. In

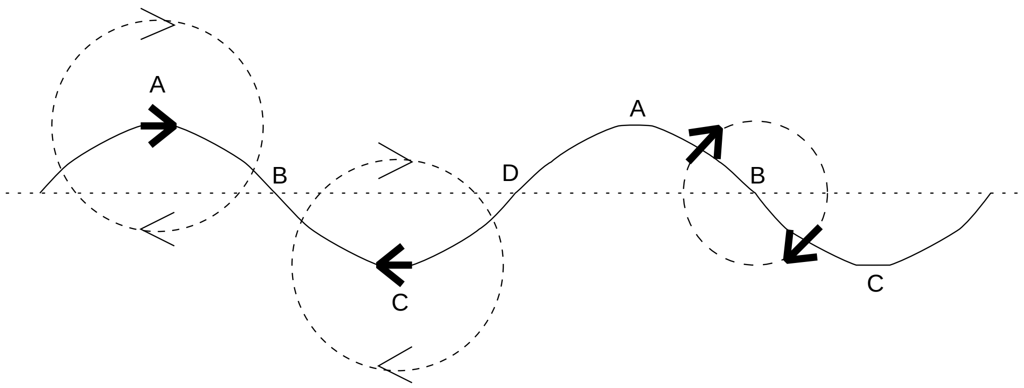

Figure 1.2: Schematic diagram showing the evolution of a sinusoidal perturbation to a vortex sheet (solid line). The background flow is to the left below the sheet, and to the right above. The left hand side of the figure indicates the flow induced at and by points like A and C. The right hand side indicates the circulation induced by the concentration of vorticity at points like B.

turn the circulation induced by (or, rather, that must exist to be in balance with) the increase in vorticity at B will lead to an amplification of the displacement of the vortex sheet, as indicated at the right of Fig. 1.2. In addition, as the disturbance grows it becomes asymmetric, forming spirals (see Rosenhead (1931) who implemented numerically the process described above, or Fig. 1.3) around points like B. The regions of overturning have been called billows, and the stretched out regions (like at D) have been called braids, although the same terms are frequently used in the radar literature to represent the whole structure.

The shear across the interface is clearly the driving force behind this mechanism. Conversely, if there is static stability across such an interface it acts to suppress the growth of any disturbance. These two effects are encapsulated by the gradient Richardson number, defined by

$$Ri = \frac{N^2}{S^2},$$

where $N^2 = -(g/\rho)\partial\rho/\partial z$ is a measure of the static stability, and $S = \partial u/\partial z$ is the vertical shear in the plane of the two-dimensional disturbance. Clearly this definition is only meaningful when the density and velocity profiles vary continuously over an transition layer of finite depth, as will be the case in any real flow. Negative values of the Richardson number imply convective instability. When evaluated over a layer of finite depth, Δz, the bulk Richardson number is given

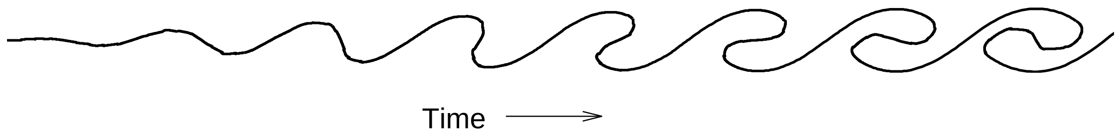

Figure 1.3: Evolution of an unstratified interface within a flow perturbed by the neutral-mode streamlines given by Miles (1963). Time increases from left to right.

by

$$Ri_B = \frac{g\Delta\theta\Delta z}{\theta(\Delta u)^2}.$$

Thus, for a given temperature and velocity change over a layer, the Richardson number evaluated over the layer is directly proportional to the layer depth. Problems with calculating the Richardson number from atmospheric observations will be discussed later.

Miles (1961) and Howard (1961) showed that a necessary condition for instability of an inviscid stratified shear flow is that $Ri < 0.25$ somewhere in the flow. This result, obtained from a linear stability analysis of the equations of motion, may also be obtained by consideration of the kinetic and potential energy consequences of the momentum conserving exchange of two fluid parcels of equal volume in a stratified shear flow (e.g. Ludlam 1967, Drazin and Reid 1981). For instability, the kinetic energy released by the exchange must be greater than the potential energy gained, which again gives the condition that for instability the Richardson number must be less than 0.25 when evaluated over the layer over which the hypothetical parcels were exchanged. However, this criterion does not give a sufficient condition for instability (although it can be shown that it is sufficient for certain background states) as for certain velocity and density profiles the Richardson number may fall considerably below 0.25 before instability sets in. For example, for a flow with a $\mathrm{sech}^2(z)$ velocity profile the critical Richardson number may be 0.214 (Turner 1973). In spite of this, it is generally assumed that the atmosphere will be susceptible to instability if the Richardson number is calculated to lie between 0 and 0.25 (Hazel 1972). This is likely to be a reasonable assumption for the profiles which tend to occur in the atmosphere.

Analytical results giving the dependence of the growth-rate on the wavelength are also of particular interest, as these then give an indication of the wavelength which is most likely to be

Missing
Figure

Figure 1.4: Neutral curves for the profiles considered by Drazin (1958) (dashed) and Miles (1963) (solid). The locus of the maximum growth-rate has been indicated for the latter. $k = 2\pi/\lambda$ is the wavenumber, and d is a vertical scale determined by the profile of velocity, which has the form tanh (z/d) in both cases. Miles used the same form for the density profile. Drazin used a simple background exponential decrease in density with height.

observed in real flows. An example of this is given in Fig. 1.4, based on Miles (1963), showing the neutral modes which separate the stable and unstable modes in Richardson number/wavenumber (k) space for profiles of velocity and density of the form $\tanh(z/d)$, where d is a length scale characteristic of half the layer depth. Fig. 1.4 also indicates the locus of the maximum growth-rate in the unstable region. The neutral curve for a background state with an exponential density variation and a tanh velocity profile is also shown (from Drazin 1958). The neutral modes may be found analytically as they have zero phase velocity, but in general the growth-rates for the unstable modes may only be found by numerical solution of the appropriate eigenvalue problem. When applying such a diagram to observations, it may be interpreted in at least two ways, corresponding to situations which may occur in the atmosphere:

- Given atmospheric profiles of static stability and wind velocity, the observed Richardson number at the center of the shear layer could be used to find the (non-dimensionalised) wavelength of the disturbance with the largest growth-rate. Given a continuum of infinitesimal perturbations in the atmosphere, this wavelength would be the one which would grow the fastest and come to dominate over the others, and thus be observed, assuming the continued validity of the linear analysis.

- Given that the atmospheric profiles of static stability and wind velocity had a specified form, but a super-critical Richardson number, if some external process acted to decrease

> the layer depth and thus the Richardson number gradually without changing the form of the profiles then the mode with the wavelength equal to the wavelength of the neutral mode at $Ri = Ri_c$ would be the mode which became unstable first. If the Richardson number varied on a time scale longer than the time-scale for growth of the billows (which is generally only a few minutes), then this is the wavelength that would be observed.

As it turns out, the fastest growing wavelength does not in generally vary much with Richardson number, and, for a given form of profile, is approximately directly proportional to the depth of the shear layer. Ratios of the horizontal wavelength of the most unstable wave to the shear layer depth, $\lambda/\Delta z$, range from around 4.4 (Drazin 1958) to 6.3 (Turner 1973) for smoothly varying profiles.

There will be significant differences in the characteristics of billows that occur in situations given by the two processes/interpretations above (at least for reasonably deep (0.5-1 km) shear layers in the atmosphere), the first referring to an arbitrarily small initial Richardson number, and the second to a sub-critical Richardson number created as a result of a gradual modification of an initially stable shear layer. This is because synoptic scale processes (e.g. Roach 1970, Keller 1989) generally act to change the Richardson number on timescales of hours, whereas billows may undergo their complete lifecycle in around 10 min. Thus, in the absence of processes acting to lower the Richardson number suddenly, even large-amplitude billows (i.e. those occurring over a large depth) occurring as a result of synoptic-scale forcing are unlikely to have strong velocity perturbations associated with them unless they exist in an environment with exceptionally strong shear, as experiments described below have shown that flows with near-critical Richardson numbers tend to overturn relatively weakly, for a given shear strength. Meso- and smaller-scale processes, such as gravity waves, density currents and some cold fronts, may have a dynamical structure which produces a rapid decrease in Ri following the flow, and thus KH instability with a very low initial Richardson number. The identification of another process which allows *intense* large-amplitude billows to occur over large distance and time-scales is one of the subjects of this thesis.

Other characteristic features of the KH mode of instability are that the phase speed of the wave is equal to the background velocity at the inflection point of the shear layer, and that the amplitude of the disturbance decreases rapidly away from the shear layer (Davis and Peltier 1976). These features have been used to associate observations of waves with KH instability in the atmosphere, in regions of low Richardson number. Additionally, in the presence of a solid lower boundary (i.e. the ground) analytical studies (e.g. Lalas and Einaudi 1976, Davis and Peltier 1976) have shown that two other effects may become important:

- The properties of the KH mode will be dependent on z_i/h, the ratio of the height above the ground of the inflection point in the shear layer to the half-depth of the shear layer. The ratio $\lambda/\Delta z$ of the fastest growing mode decreases with z_i/h, although it remains within the range of values mentioned above. Also, the growth-rate of the fastest growing mode decreases rapidly for $z_i/h < 4$, and becomes zero at $z_i/h = 0.9$ (for the background profiles used by Davis and Peltier (1976)). The vertical structure of the wave, described by the magnitude of the vertical velocity perturbation, is altered considerably by the close proximity of the ground, resulting in a strong asymmetry above and below the shear layer. These effects will be discussed again with reference to the observations described in Chapter 3.

- Trapped and propagating resonant modes become possible, with wavelengths longer than the KH modes. Waves travelling downwards away from the shear layer reflect off the ground, and interfere with the upwards travelling wave to form a standing wave pattern between the ground and the shear layer. Davis and Peltier (1976) proposed that sub-critical Richardson numbers generated at the nodes in this standing wave pattern could generate small-scale KH instability and thus explain the multiple thin layers which have been observed in the boundary layer. However, as such modes have much lower growth-rates than the KH modes, they are unlikely to develop, unless non-linear effects become important, or the waves can grow from a finite amplitude disturbance, perhaps generated by KH vortex pairing in the original shear layer (Davis and Peltier 1977).

Thorpe and Holt (1995) described the effect of a slope of the lower boundary in a direction perpendicular to the shear vector using both analytical and experimental methods. Although in the main case study presented in this thesis there was some slope of the shear layer relative to the

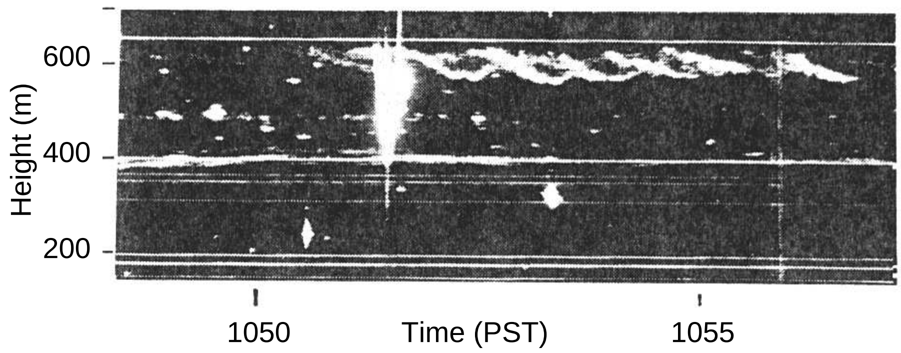

Figure 1.5: Example of a clear-air reflectivity time-height display showing the braided and cats-eye structure characteristic of atmospheric KH billows (from Gossard 1990).

ground as a result of the structure of the frontal zone, the magnitude of this slope was sufficiently small that it was unlikely to have had any significant effect on the properties of the billows that developed.

1.3.2 Atmospheric observations of KH billows

Radar observations

Since the early 1970s, many radar observations have been made of KH billows in the atmosphere. Most of these have been of billows occurring in the clear air, visible to high-power radar as a result of refractive-index inhomogeneities caused by the billow structure. The reflectivity pattern that occurs is sufficiently characteristic of KH billows (e.g. Fig. 1.5) that it may be considered to be a signature, as it has never been reported in any other context.

The two most straightforward and testable results of linear theory, namely the existence of a critical Richardson number and a strong relationship between the wavelength (λ) and crest-trough amplitude (Δz), have been verified in many cases. One of the difficulties in making and interpreting these observations is obtaining thermodynamic and wind profiles through a stratified shear layer just *before* the onset of finite-amplitude billows, which may then be detected by radar. If the profiles were obtained from radiosonde ascents the non-representativity of the measurements may be significant, as an ascent through a layer actually containing billows would show a gradient

Richardson number profile highly dependent on whether it went through the billows core or braid. The bulk Richardson number, calculated over the whole layer, would also be affected due to the mixing induced by the billows. However, on 17 separate occasions, Browning (1971) found that the Richardson number obtained from radiosonde ascents in the vicinity of KH billows of amplitude 200-450 m, fell within the range 0.15-0.3 when calculated over depths of 200 m. This is consistent with a critical Richardson number of around 0.25. The ratio of λ to Δz was found to vary considerably, between 2 and 10. However, since the radar observations (from which these ratios were derived) were not necessarily made in directions perpendicular to the orientation of the billows, some of these are likely to have been over-estimates.

Other observations of billows in the clear air give similar results. Hicks and Angell (1968), who originally drew attention to braided reflectivity structures in the clear air, observed billows on at least 9 out of 23 observing days, with $\lambda/\Delta z$ having a mean value of 4. Browning *et al.* (1973a) observed billows with $\lambda/\Delta z = 2\text{km}/0.4\text{km} = 5$ in a layer with $Ri \approx 0.25$. Hardy *et al.* (1973) found $\lambda/\Delta z = 2.7/0.5 = 5.4$ and $Ri \approx 0.15$ in the layer containing billows.

A few Doppler radar observations of billows occurring in precipitating regions have also been reported. Browning *et al.* (1970a) investigated the occurrence of shearing instability in precipitating frontal regions, although the actual structure of billows was not their main focus. Bryant and Browning (1975) inferred the presence of KH billows with a wavelength of 1 to 2 km from vertical profiles of mean and variance quantities derived from Doppler radar data within a precipitating frontal zone. Wakimoto *et al.* (1992) observed KH billows over a layer 870 m deep using air-borne Doppler radar just ahead of a very intense surface warm front. Observations very similar to those described in this thesis were reported by Takahashi *et al.* (1993), who made measurements of 3.5 km wavelength billows within a precipitating stationary frontal zone. In this latter case, the billows were also clearly visible in the reflectivity field, as adiabatic warming in the downdraft regions of the billows caused melting of ice particles, effectively creating a locally enhanced bright band. However, in general the reflectivity field does not seem to indicate the presence of billows unless they are sufficiently vigorous to produce significant vertical velocity perturbations which alter the precipitation number-density distribution. Chapter 2 goes some way to explaining the lack of radar observations of billows in precipitating regions.

Non-radar observations

Non-radar observations of KH billows in the atmosphere have also been made, especially in the boundary layer. Although only radar (or sodar/lidar) measurements are capable of providing near-simultaneous high-resolution measurements of the velocity field within billows, measurements made from aircraft or instrumented towers have the advantage that velocity, including turbulence correlations, and thermodynamic data may be obtained simultaneously. For example, Blumen (1984) made turbulent flux measurements from an instrumented tower of KH billows occuring at the top of a night time drainage flow. Nielsen (1992) observed billows within a coastal front inversion using aircraft measurements.

KH billows may sometimes be observed visually if they either create or modify clouds. Ludlam (1967) reported a number of such observations, and was able to relate their location and height to profiles derived from radiosonde ascents, showing that they occurred at levels where the Richardson number was close to 0.25.

1.3.3 Evolution and breakdown of billows

The evolution of the billows beyond the initial infinitesimal perturbation can, in general, only be analysed using numerical simulations or observations. Early numerical simulations by, for example, Patnaik *et al.* (1976), were done in two dimensions only, because of the limitations of computing resources. These gave reasonable results for the initial stages in the billow evolution, showing, amongst other things, that the overturning of isopycnics is much weaker for flows with a larger Richardson number — overturning only just occurring for $Ri_{min} = 0.15$ (with $Re = 100$). However, attempts to model the behaviour at later stages have limited applicability in the atmosphere because of the inability of a 2D model to represent 3D motions that more recent experiments have shown may occur. Two dimensional simulations by Davis and Peltier (1979) showed very high Rayleigh numbers in the convectively unstable billow cores, so Sykes and Lewellen (1982) attempted to model the billow breakdown and transition to turbulence by using a second order closure scheme to describe the 3D small-scale turbulence field within a 2D model. These calculations showed the correct qualitative behaviour (compared to laboratory tank experiments by Thorpe (1973a)) of the evolution of the billows over their lifecycle, and indicated that the final Richardson number of the layer is raised above Ri_c, by deepening the transition layer depth. Sykes and Lewellen also showed how the regions of high temperature variance (and, by implication regions of high refractivity variance) through the billow evolution were consistent with the clear-air radar observations of the lifecycle of a train of billow by Browning and Watkins (1970).

A significant difference between the model/laboratory tank experiments described so far and atmospheric radar observations is that Browning and Watkins found that both reflectivity (and thus by implication the stratification) could be split into two distinct layers by KH billows. Hourly radiosonde ascents showed a similar split in the stratification and Richardson number (though not in the shear) which continued to exist for over two hours after the billow event. In contrast, Sykes and Lewellen (1982) and Thorpe (1973a) found that the final state had a single peaked, low (but super-critical) Richardson number over the layer. However, more recent 3D simulations (Scinocca 1995, Fritts *et al.* 1996a) have showed a split in the final stratification and shear profiles, lending support to the observations by Browning and Watkins. The nature of the final state is important, as it is generally assumed (if taken account of at all) in NWP models that the effects of KH instability will be purely diffusive. Splitting of a single layer into multiple layers, which might themselves become dynamically unstable, might have a qualitatively, and possibly quantitatively, different effect on the mean profiles.

Laboratory experiments by, for example, Thorpe (1973a), which demonstrated the existence of small-scale motions in the billow core associated with the onset of turbulence prompted Klaasen and Peltier (1985b) to test the stability of 2D finite amplitude billows to 3D infinitesimal disturbances, finding that the most unstable modes exist in the spanwise plane. Thus they may take the form of counter-rotating vortices, with axes lying in the streamwise plane, in the convectively unstable regions of the billow core (see Fig. 1.6). A condition for the growth of such modes is that the Reynolds number is above a critical value, which itself depends on the details of the wave structure (and thus the initial conditions), but is around 220 ± 50. Thus this mode may well be relevant in the evolution of atmospheric billows, where the Reynolds number may be

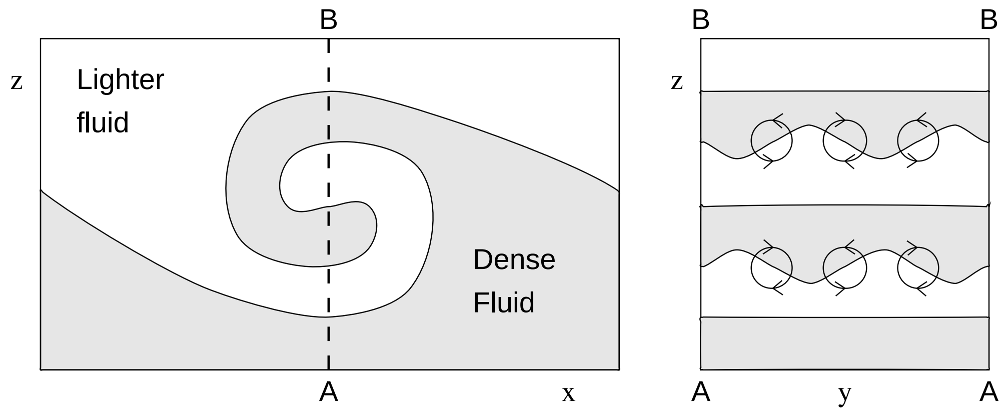

Figure 1.6: The left-hand diagram shows the KH billow in the streamwise ($x - z$) plane at a time when the overturning in the billows core has produced two regions of static instability. The right-hand diagram shows how this secondary instability is released in the spanwise ($y - z$) plane, containing the line AB, in the form of counter-rotating vortices. The horizontal scale of the secondary instability is actually around one tenth of the KH wavelength.

much larger than this critical value. Further (non-linear) development of these structures mixes fluid within the billow cores, and leads to their eventual breakdown and return to parallel flow.

The existence of secondary convective structures in real flows has been demonstrated by Thorpe (1985) using shadow-graph images of KH billows in laboratory tilted-tank experiments. The ratio of the wavelengths of the secondary instability to that of the KH instability ranged from 0.15 to around 0.05, the latter being for higher Reynolds numbers of around 1500. These results are consistent with the theoretical predictions by Klaasen and Peltier (1985a). Thus, even for large-amplitude atmospheric billows with a wavelength of, say, 5 km, the secondary disturbances would only have a wavelength of at most around 500 m. This would require a radar resolution of 250 m or better to resolve them. Given the high angular resolution of Chilbolton radar, this may be possible using scans at high elevation angles, although the range resolution, which is 300 m with the present configuration, is probably too poor to make such measurements. Metcalf *et al.* (1970) were able to make ultra-high resolution (2 m) clear-air radar reflectivity measurements of KH billows which had an amplitude of around 150 m, and noted the occurrence of secondary instabilities at the peaks (and troughs) of the billow cores. However, the appearance of secondary instabilities did not seem to prevent further amplification of the primary billows, in one case the amplitude apparently tripling before the wave structure was destroyed. James and Browning (1981) obtained Doppler velocity spectra within a train of billows, and interpreted localised features within the billows cores as secondary KH disturbances growing on the backs of the primary billows. However, the nature of the measurements would allow a number of alternative explanations, so, like the observations by Metcalf *et al.*, do not decisively indicate the structure of the secondary disturbances, only their existence. Ludlam (1967), in his analysis of billow clouds, noted the appearance of a pattern orientated perpendicular to the billows just before they dissipated. This pattern had a wavelength approximately one fifth that of the primary billows and is, perhaps, consistent with the secondary instability which has been described.

Given the inability of analytical methods to reveal the evolution and eventual effect of these secondary instabilities, and the difficulties in obtaining quantitative and unambiguous observations in both laboratory experiments and the atmosphere, numerical models seem to provide the most reliable and flexible means of investigation. However, 3D simulations are computationally very expensive, and have only recently been performed (e.g. Scinocca 1995, Fritts *et al.* 1996a). The structure of the instability, which first appears when the billows have reached their maximum amplitude, has been described by Scinocca who shows iso-surface plots of the mass-density surface which are essentially as indicated in Fig. 1.6. Chapter 3 discusses further the role these secondary instabilities play in influencing the evolution of the main KH billow as the details are directly relevant to the momentum flux calculations shown there.

Up until this point this discussion of the processes by which KH billows break down and return to laminar flow has concentrated entirely on the convective instability of the core. However, there are a number of other processes, mainly observed in laboratory tank experiments, which may occur as well:

- Vortex pairing has been studied using numerical models (Patnaik *et al.* 1976) and laboratory experiments (Scotti and Corcos 1972, Koop and Browand 1979) but, to the author's knowledge, has not been reported in atmospheric observations. This is perhaps because for vortex pairing to occur the stratification external to the shear layer must be weak, as otherwise there is insufficient energy available to supply the potential energy needed to locally double the layer depth. If it occurred it would, presumably, be quite distinctive and resolvable by any radar method capable of resolving the KH billows. A non-linear interaction with resonant waves (mentioned above) means that it could, in some situations, be a significant process (Davis and Peltier 1979).

- Secondary dynamic instability within the braids (Maslowe 1973) as inferred from radar observations by James and Browning (1981), although this has been observed *not* to occur by Thorpe (1985).
- "Knots" (Thorpe 1985) occur when the billow cores, which extend in the spanwise (y) direction, meet at some location (effectively a localised vortex pairing event). Thorpe (1985) shows small-scale turbulence developing in locations where this occurs.
- Vortex "tubes" (Thorpe 1985) may develop on the braid between one billow and its neighbour when the extent of the billows is significantly great in the spanwise direction. These again may locally accelerate the onset of small-scale turbulence where they attach to the billow cores.

The latter two processes have not been studied using numerical models, because to do so would require a large domain containing more than one billows wavelength, as well as high resolution. Whilst knots may be fairly easy to identify in radar data (perhaps using analyses such as in Fig. 3.2), vortex tubes are unlikely to be resolved by the radar. Some insight might be obtained by making use of Doppler spectra, as James and Browning (1981) did. In their case they did not observe large values of the spectral width in the braids, indicating that in that case vortex tubes were not occurring. It thus seems likely that convective instability is the predominant mechanism for the breakdown of billows in the atmosphere, though whether it occurs in the highly organised manner indicated in numerical and laboratory models is not clear.

1.4 Motivation for the present study

There are a number of subject areas that would benefit from a better knowledge of the occurrence and properties of KH billows in the atmosphere. They include the following:

- Prevention of the collapse of fronts/shear zones. Browning *et al.* (1970a) showed that frontal zones, existing in a flow field acting to reduce their thickness and Richardson number, contained billows which acted to smooth vertical gradients and thus prevent the collapse of the front. Thus the existence of billows relates the thickness of such shear zones to some limiting Richardson number, between 0.25 and 1. The lack of explicit representation of Richardson number dependent mixing in the free atmosphere in some numerical weather prediction models may therefore be a serious omission.

- Vertical mixing of chemicals/pollutants. The tendency for KH billows to occur in frontal zones means that chemical constituents may be transferred from one air flow to another, and thus be transported rapidly from, say, the boundary layer to the upper troposphere. It also provides a mechanism for bringing together a variety of chemical species from different sources (e.g. the boundary layer and the upper troposphere/lower stratosphere) which may then react, affecting the distribution of chemicals in the free troposphere.

- Dissipation of kinetic energy. Trout and Panofsky (1969) showed that the dissipation of energy by CAT at upper levels in the troposphere was sufficient to have some significance in the dynamics of the local atmospheric circulation. A similar result may be expected if a quantitative study were to be carried out investigating the effects of billows at lower/mid levels, including those occurring in precipitation.

- VHF radar measurements of the mean vertical wind. Vertically pointing VHF radars are used to measure profiles of the vertical velocity and its long-term mean (in the clear air). Muschinski (1996) showed that, within KH billows, variations in refractivity-surface tilting angles are correlated with fluctuations in the vertical velocity measured by the radar, which can lead to a bias in the measured vertical velocity with a magnitude of several tens of centimeters per second. This may lead to systematic errors in the vertical velocities measured around jet streams or other structures which have been associated with billows.

- Aviation safety. KH billows have been shown to be a significant cause of Clear-Air Turbulence (CAT) (Browning *et al.* 1970b), a source of inconvenience and possibly danger to aircraft (see Knox 1997). Although the majority of CAT reports come from aircraft flying at high altitudes, the observations described in this thesis show that KH billows also occur at low levels, and act to locally concentrate the vertical wind shear as well as create localised regions of significant vertical velocity. These effects could be especially relevant for aircraft taking off and landing.

The points above are addressed more fully in the appropriate parts of the thesis. The observations described in this thesis are also of interest because it is important to know what structures and properties are associated with KH billows, so that when they occur in association with some other larger-scale process, their effect and relevance may be determined.

Although this thesis is based mainly on a single case study, a number of other cases are presented briefly in Chapter 2 in order to provide examples of the use of displays of the vertical shear in detection of KH billows using Doppler radar. The main case-study is presented in Chapters 3 and 4. Chapter 3 concentrates on the radar observations of billows in a warm frontal zone, discussing their structure, lifecycle and effect on the mean flow through momentum fluxes. Chapter 4 uses the Met. Office UM to determine the front's thermodynamic and flow structures that were responsible for the billows' existence and properties. This leads to the recognition of a more general process which we have called potential shearing instability. Chapter 5 summarises the main conclusions, and makes suggestions for ways in which this work could be extended.

CHAPTER 2
Doppler radar observations of billows

2.1 Introduction

There have been few published radar observations of KH billows in precipitation, and it might be inferred from this that KH billows occur very rarely in such regions in the atmosphere. The aim of this chapter is to provide the motivation for the more detailed study in the following chapters, by showing that they occur frequently in certain precipitating regions, and must have been overlooked in many previous studies using radar.

2.2 Use of RHIs showing vertical shear

RHIs of Doppler radar data are usually visualised using colour shading to represent velocity. Although in general this clearly shows extrema in the data, it is very difficult to judge the magnitude of the velocity gradient in either the horizontal or the vertical, and it is even harder to tell if there is a pattern in this gradient field. However, when combined with the original Doppler velocity field, RHIs (Range Height Indicators) showing the vertical derivative of the Doppler velocity reveal patterns indicative of dynamical processes that would otherwise remain hidden.

Horizontal derivatives giving, for example, horizontal deformation and divergence, are occasionally displayed in the form of RHIs and time-height plots of Doppler radar data. However, there have been few publications showing RHIs of the vertical derivative of the Doppler velocity (vertical shear) and they have all been related to observations of KH billows. Starr and Browning (1972) showed the numerical values of the vertical shear calculated over 200 m height increments within billows which had a crest-trough amplitude of around 600 m. Browning *et al.* (1973a) showed the vertical shear calculated over 100 m height increments through billows which had a crest-trough amplitude of between 230 and 450m. Although both these studies showed that the shear had maxima in the billows themselves, the resolution of the measurements (compared to the amplitude of the billows) was insufficient to resolve details in the patterns of shear. Weckworth and Wakimoto (1992) showed vertical cross-sections derived from a multi-Doppler analysis of the horizontal vorticity (i.e. containing the appropriate component of the vertical shear) parallel to the axes of a train of KH billows, unusually orientated perpendicular to the density current-like front in which they occurred. Again, although they used the vorticity maxima to indicate the locations of the billows, the resolution of the data, degraded after interpolation onto a 500 m resolution grid, is insufficient to show any structure to these maxima. Recently Chapman and Browning (1997)[1] showed the shear calculated over height increments much smaller than the amplitude of the billows through which the measurements were made. These shear RHIs, obtained within frontal precipitation, show cats-eye and braided patterns that are very similar to the clear-air reflectivity "signatures" of KH billows (see, for examples, the review by Gossard 1990).

James and Browning (1981) showed time-height sections of vertical shear, calculated from high-resolution radar observations made at a fixed elevation angle of 60°, through only the upper half of a train of billows. Although in retrospect the patterns seen by Chapman and Browning (1997) can be seen in their data, at the time the structures were not noticed, perhaps because observations were not available over the whole depth of the billows. Brown and Rogers (1997) noted multiple shear layers in wind profiler data, possibly associated with gravity waves. However, the resolution of wind profiler data is insufficient to resolve structure due to KH billows.

The term "vertical shear" as used here refers to the vertical derivative of the Doppler velocity, evaluated at low elevations and constant range. Thus the component of vertical shear in the plane of the RHI, as shown in the figures in this thesis, is given by

$$S_{i,j} = \frac{\partial V}{\partial Z} \approx \frac{V_{i,j+1} - V_{i,j-1}}{Z_{i,j+1} - Z_{i,j-1}}$$

where V is the Doppler velocity, Z is the height of the scanned volume, and the subscripts i and j

[1] which forms the basis of part of Chapter 3

refer to slant range (i.e. range along the beam) and elevation angle, respectively. For observations made using the Chilbolton radar elevation spacings of $0.25°$, S is evaluated over a vertical distance given by $\Delta Z \approx 10 \times Range$ where the height and range are measured in meters and kilometers, respectively. The resulting shear has been smoothed to a small degree using a nine-point moving average around each point. This has been used to reduce the effect of noise which is amplified when derivatives are calculated, although generally this was not found to be a problem. There is a small error in the expression for S because for non-zero elevations it includes a component of the horizontal gradient of V. This error could be eliminated, although it would result in a more complex expression for the difference approximation. Since this error is appreciable only at large elevations we have neglected it in this study.

2.3 An example of shear structures within upper cold fronts

The main aim of this section is to show that features which are clearly visible in RHIs showing the vertical shear may be almost completely invisible in the original Doppler velocity RHI. This is particularly true for KH billows, which give rise to a characteristic signature in the shear.

Figure 2.1(a) shows a Doppler RHI through two upper cold fronts which over-ran a surface warm front (SWF) on 5 January 1998. Each upper cold front has a thermally direct circulation associated with it, as indicated by the colour shading which has been chosen so that blue represents descending cold air moving away from the radar, and red represents ascending warmer air moving towards the radar, relative to the cold air. The structure is similar to that described by Browning *et al.* (1973) (see Fig. 8 of their paper for a schematic diagram of the processes occurring).

The Doppler velocity field is smooth, which would seem to imply that strong mixing is not occurring between the cold and warm air. However, close inspection of the data between ranges 45 and 55 km at a height of around 3 km, does show some weak wave-like perturbations to the velocity field. These perturbations are much clearer in the shear RHI in Fig. 2.1(b), and appear as braids and cats-eyes. The similarity of these structures to braids and cats-eyes observed previously in clear-air radar data (e.g. Fig. 1.5) indicates the existence of KH billows which were mixing

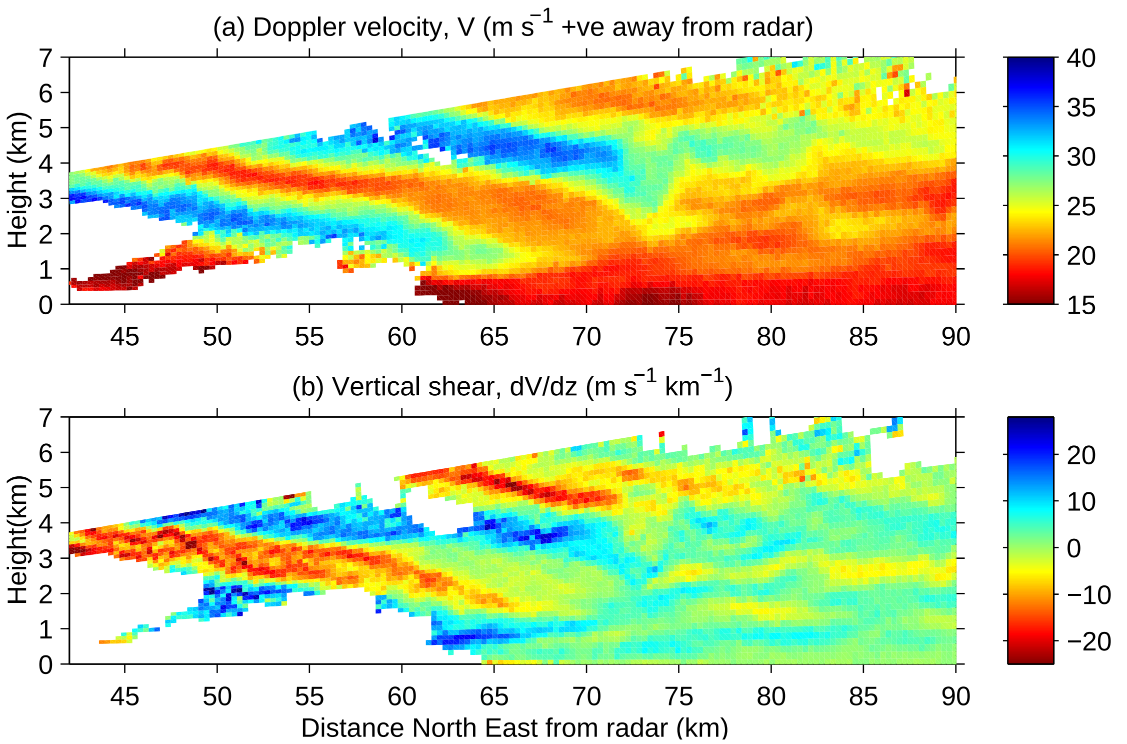

Figure 2.1: RHIs from Chilbolton radar at 1118 UTC on 5 January 1998 at an azimuth of 47°. (a): Doppler velocity, V (m s^{-1}). (b) Vertical shear, $\partial V/\partial z$ (m s^{-1} km^{-1}).

air over a depth of 1 km at the statically stable transition zones between the descending cold and dry upper-tropospheric air, and the ascending warm and saturated lower-tropospheric air. Similar structures existed for the next 30 minutes, until this region had moved too far away from the radar for them to be resolvable. Four separate frontal circulations were sampled by the radar during the observation time. Shear structures also existed in some of the other transition zones associated with these circulations, though they were less distinct, and data were not available in some regions because of evaporation of the precipitation as it fell through the cold, dry air.

The mixing induced by billows is likely to have been of importance in terms of the effect on thermodynamic profiles as it occurred at the boundary separating air with very different properties and origins. It is also of potential importance in bringing together different chemical species which may then react influencing the distribution of chemicals in the free troposphere.

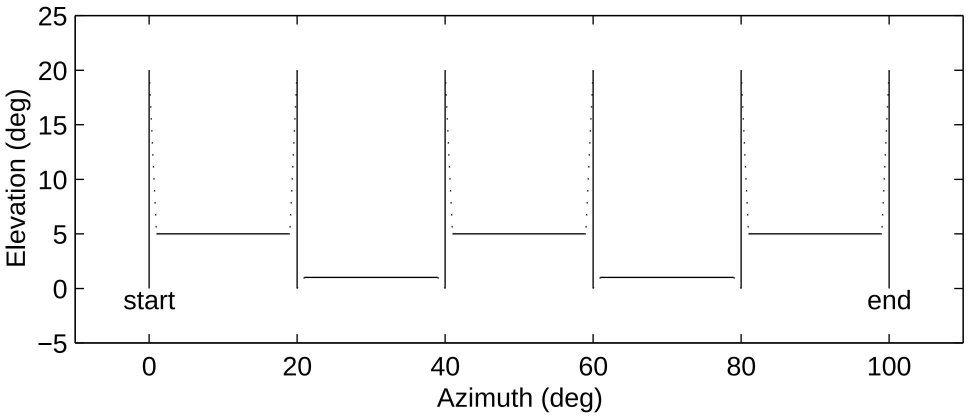

Figure 2.2: Example of a FASTEX scanning sequence. The solid lines indicate radar scans where data was recorded, the vertical and horizontal lines representing RHIs and PPIs, respectively. Dotted lines indicate where the dish was moved with no data being recorded. It takes approximately 7 minutes to complete the sequence shown, and a further 100 seconds to return to the start position.

2.4 Mixing associated with fronts during FASTEX

The Fronts and Atlantic Storm Track Experiment (FASTEX) (Joly *et al.* 1997) occurred during January and February 1997. Intensive observations were made of storms and fronts as they developed over the Atlantic, some of which then moved over the UK. During this experiment, the Chilbolton radar was scanned frequently using automated scanning sequences, obtaining RHIs and PPIs (Plan Position Indicators) alternately (see Fig. 2.2 for an example) through the majority of precipitating frontal regions that passed over the radar between 4 and 25 February. However, the range of azimuths used in the automated scans was typically around 90° and centered on an azimuth perpendicular to the surface front. Thus, in general data were not available in directions parallel to the surface front, which is the direction of the thermal wind shear. As a result, this dataset must underestimate the frequency of billows which occur as a result of the thermal wind shear, as they would only be visible to the radar if they were exceptionally intense. In addition, cold fronts were scanned in preference to more weakly precipitating warm fronts, and regions in which to scan were chosen on the basis of strength of precipitation rather than the likelihood of billows occurring. These factors all indicate that the dataset is likely to underestimate the occurrences of billows occurring in frontal regions associated with cyclones over the UK during winter.

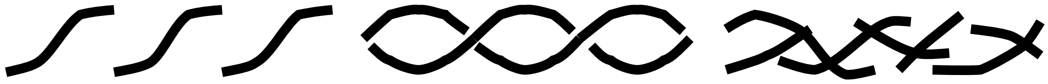

Figure 2.3: Classification of the structures observed frequently within vertical shear RHIs. The lines show the patterns of maximum shear. Braids, cats-eyes and a turbulent layer are represented in (a)-(c), respectively.

However, bearing this in mind, it is still interesting to look at the occurrences of shear features in the dataset. The results are as follows (see Table 2.1):

- The vast majority of data were from the vicinity of fronts, with a clearly defined vertical shear direction over the depth of the front. Those data (from only a few days) that did not show this have been disregarded in the following paragraphs, as their inclusion would only confuse the points made.
- The majority of the RHIs did not show a single vertical layer over which all the shear (and presumably stability) was concentrated. Instead they showed multiple shear layers on vertical scales of around 1 km.
- Although many of these shear layers remained “laminar” (to the resolution of the radar) for much of the observing time, in *every* observation period (normally lasting a few hours) there were some RHIs in which the shear layers showed “structure” to some degree. This structure consisted of distinct shear patterns, which were coherent over a number of scanning volumes, rather than simply random fluctuations from one range/elevation gate to the next. Unfortunately it has not been possible to quantitatively determine any meaningful frequency or duration of these features from the data available for reasons mentioned above.
- The shear layers in which this structure was observed were classified according to Fig. 2.3. In addition, a subjective estimation of the strength and clarity of braided/cats-eye structures was made, where relevant. Under this scheme, the structures in Fig. 2.1, for example, would be classified as cats-eyes with medium strength/clarity. Table 2.1 shows that the braids and cats-eyes all had a vertical extent less than or equal to around 1 km. This appears to be true of all reported observations of KH billows in the atmosphere. Billows of 1 km vertical extent appear to be surprisingly abundant in the data compared with still-resolvable billows

Date	Obs. Times	Br	C-E	Depth	Synoptic situation
4	1000-1023	-	-	-	Ahead of SCF, behind SWF
4	2300-2330	s	-	0.5	Above SCF
7	1050-1600	m	w	1.0	Just behind SCF
10	0800-1343	m	w	0.7	Ahead of SCF
11	1200-2010	s	s	1.0	Just ahead of SWF
11	2230-0154	-	-	-	Behind SWF
12	1750-2110	w	-	-	At/behind SCF
13	0030-0330	m	w?	1.0	Behind SCF
14	0845-1349	m	-	0.4	Close to SWF and SCF
17	1830-2230	w	w	0.8	Behind SCF
19	1624-1727	w	-	1.0	At/behind SWF
21	0845-1015	m	-	0.4	Behind SCF/in front of SWF
24	1445-1840	s	m	1.0	Close to SWF and SCF
25	1640-1900	m	w	1.0	Behind SCF

Table 2.1: The occurrences of braids (Br) and cats-eyes (C-E) (as indicated in Fig. 2.3) within shear layers in the vertical derivative of Doppler data from Chilbolton radar during February 1997. The times relate to the period of observation, not to the duration of the features (most were only observed for a short time relative to the total observation period). The letters w, m and s (weak, medium and strong, respectively) refer to a subjective estimation of the strength/clarity of the relevant feature. The depth (in km) refers to the approximate vertical extent of the feature/shear layer. The synoptic situation relates to the time at which the "most interesting" features occurred.

of, say, half this amplitude. "Turbulent layers" were observed above the boundary layer in all the observing periods.

- The majority of occurrences of braids or billows occurred actually within or on the edge of frontal zones, and were not merely loosely associated with them, as in the case shown later in Fig. 2.4(c).

Even though none of the individual cases in this dataset have been studied in great depth, the results clearly show that frontal zones often contain multiple shear layers, and that these shear layers frequently show evidence of mixing as a result of KH billows. Neither of these conclusions would have been expected as a result of most other radar observations in precipitation, although multiple layers of enhanced shear have been observed in clear-air wind profiler observations by (e.g Brown and Rogers 1997) who claimed that the layers, which were regularly spaced up to around 3 km in height, were caused by a gravity wave. Multiple layers of other properties have been frequently reported. For example, Chilson *et al.* (1997) observed many thin scattering layers (and also KH instability) around an upper-tropospheric jet. Sato and Woodman (1982) observed multiple thin layers of enhanced reflectivity, wind-shear and spectral width in the stratosphere using a vertically pointing radar. Gage (1990) and Gossard (1990) discuss observations of layered structures and possible mechanisms for their creation in the free atmosphere and the boundary layer, respectively. Woods and Wiley (1972) suggest that in the ocean the occurrence of KH instability in a stratified shear layer, rather than simply diffusing the shear and stratification profiles, may generate multiple layers by forming a well-mixed region at the center of the original layer, and a two new stratified sheared layers at the boundaries. These new layers may then develop instabilities and go on to successively generate further layers.

2.5 Use of vertical shear layers to validate/improve streamline analyses

This section will briefly describe the way in which the two-dimensional wind field may be derived from the Doppler velocity when the flow is two-dimensional. This analysis may be validated and/or improved if the flow is such that extensive, well-defined shear layers exist. A case of intense line convection is used as it also provides another good example of KH billows being visible in shear displays, but not in the original Doppler display.

2.5.1 Shear layers and streamlines

Figure 2.4(a) shows a Doppler velocity RHI perpendicular to a rather two-dimensional cold front in which near-vertical line convection occurred at the surface front (at 20 km range). The front itself was orientated due south-north, and moved eastwards at around 15 m s^{-1}. This front and its environment has been described by Browning *et al.* (1997) who derived front-relative streamlines, defined (assuming two dimensional flow, with no divergence into the plane) by

$$\frac{\partial \psi}{\partial z} = \rho u,$$

where ρ is the density of air, with the boundary condition $\psi = 0$ at the ground. The x- and z-axes point eastwards and upwards, respectively. However, here we have derived the streamlines in Fig. 2.4(a) instead by integrating downwards assuming essentially horizontal flow above the front at 6 km. The streamfunction is zero on this upper boundary, which was chosen to be sufficiently high that it was above the regions of significant vertical velocity, yet low enough to have only a small region below it in which data were not available. Velocities in this region were reconstructed using averages of the surrounding values. Integrating downwards from an upper boundary in this way reduces slightly the problems of error growth associated with the decrease in density with height when integrating upwards. The resulting streamlines in Fig. 2.4(a) indicate that cold air approached the surface front from the west, then ascended and receded to the west. Warm air approached the front from the east, rose at the surface front, then continued to flow to the west, ascending gently over the cold air.

In Fig. 2.4(b) we use the pattern of vertical wind shear as a guide to validate the independently-derived streamline pattern. The justification for being able to do this is as follows. For two-dimensional, inviscid, non-rotational flow in which the background density remains constant with height, the component of vorticity lying in a vertical plane (i.e. $\eta = \partial w/\partial x - \partial u/\partial z$) is conserved

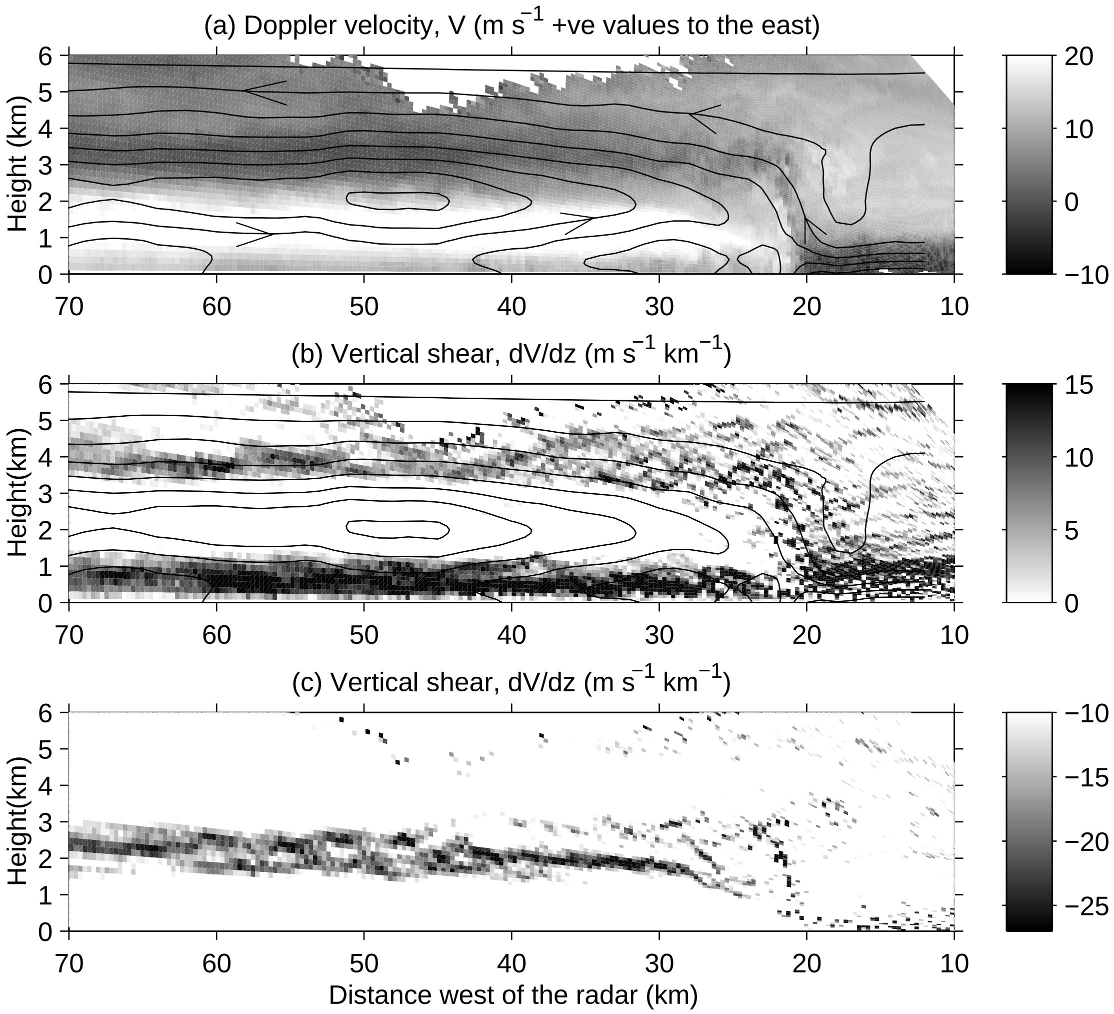

Figure 2.4: Data from Chilbolton radar at 1844 UTC on 24 October 1995 at an azimuth of 270°. Note that west is to the left of these plots. (a): Doppler velocity, V (m s^{-1}). (b) Positive values of vertical shear, $\partial V/\partial z$ (m s^{-1} km^{-1}), as defined in the text. (c) Negative values of vertical shear. A mass-weighted streamfunction (intervals of 4 kg m^{-2} s^{-1} km) derived from the Doppler velocity data has been used to overlay (a) and (b).

following the flow. This is as a result of there being no stretching/compression of vortex tubes into the plane. Thus, for steady flow, contours of the component of vorticity lying in the plane would indicate the orientation of streamlines, as flow would be along contours of the vorticity. In practice, a layer of enhanced vorticity, which will also indicate the orientation of streamlines even if the background density varies with height, will be easier to identify and follow if shading is used to represent the vorticity. For most parts of the flow, except near the line convection and where the cold air reverses direction, $\partial w/\partial x$ is considerably smaller than $\partial u/\partial z$, so the orientation of a layer of vertical shear on its own will give a good indication of the orientation of the streamlines. The main reason for non-conservation of vorticity in two-dimensional flow is likely to be dissipation, especially in any strong shear layer. However, to a first approximation the dissipation will simply spread the shear in the vertical, so it will still be appropriate to use the layer to indicate a streamline, so long as the flow is steady.

Figure 2.4(b) shows shaded just the positive values of the vertical shear, with the streamlines superimposed. Although there was some deformation at the front, resulting in non-conservation of the component of vorticity in the plane, the near-zero values of vertical velocity at low levels (calculated from the streamfunction) implies this was small. As a result, the diffuse shear layer which extends across the domain at a height of about 1 km ahead of the surface front and then rises by 20 km range to around 4 km behind the front, is a good indicator of a streamline following air that rises just above the frontal zone. There is good agreement between this shear layer and the previously-derived streamlines which lie close to it, indicating that the assumptions used in the derivation of the streamlines were justified. Note that the region of strong easterly flow (dark shading in Fig. 2.4(a)) also follows the streamlines of the ascending flow, indicating approximate conservation of this component of momentum within the flow. In cases where appropriate boundary conditions cannot be imposed (perhaps due to lack of data near the ground), a shear layer as shown in Fig. 2.4(b) could be used to define a streamline, and the remaining streamlines could be obtained by integration away from it.

2.5.2 Shear structures

Chapman and Browning (1997) showed that the shear within large-amplitude billows that were clearly visible in the Doppler returns from frontal precipitation had a cats-eye structure which was similar to the clear-air reflectivity patterns observed by, for example, Hicks and Angell (1968) and Browning (1971).

Figure 2.4(c) shows shaded just the negative values of the vertical shear, i.e. that component associated with the under-cutting by the cold air of the warm air above. The shear shows patterns at a height of 2 km between ranges 40 and 60 km that are very similar to cats-eye structures observed by, for example, Hicks and Angell (1968) and Browning (1971). There are other very shallow layers of negative shear at other heights in Fig. 2.4(c), especially between 10 and 40 km range, but we are concerned only with the more significant layer of negative shear which shows up boldly in Fig. 2.4(c) centred at a height of 2 km. The cats-eye pattern at 40 to 60 km range could be clearly seen in a similar location relative to the front in a number of other RHIs at different times. It has a crest-to-trough amplitude of 1 km and a wavelength of around 4 km, so in these terms could be described as a train of large-amplitude billows. However, the intensity of the shear is sufficiently weak that the velocity perturbation is too small to be detected easily in the original Doppler field.

Assuming that the pattern in the shear layer is the result KH billows, the location relative to the streamline pattern is such that they would have been mixing *within* the weakly stratified cold air mass rather than at its boundary. Thus they are unlikely to have had a significant effect on the thermodynamic structure of the front, although they would have affected the kinematic structure by redistributing the shear.

To the extent that the front is similar in structure to a density current, KH billows might have been expected close to the "head" between the cold and the warm air flows (i.e. between range 25 km, height 3 km and, say, range 50 km, height 5 km) as in Figs. 5 and 6 of Xu *et al.* (1996). However, the lack of any distinct cats-eye structure in this region indicates that large-amplitude KH billows were *not* occurring here, so there was less large-scale mixing across this front than might be expected from a comparison with models of density currents.

2.6 Conclusions

This chapter has demonstrated the utility of looking at RHIs of vertical shear in addition to RHIs of Doppler velocity, especially for the identification of regions containing KH billows. It appears that RHIs of the vertical shear may be used to detect KH billows in regions of precipitation in the same way that reflectivity from high-power radars has been used in the past to detect KH billows in the clear-air. This ability to confidently infer the presence or absence of KH billows makes it possible, in principle, to obtain a climatology of billows in regions of precipitation as well as in the clear air, although the FASTEX dataset available was not suitable for this to be done.

From the results of the preliminary study presented here, it appears that KH billows occur considerably more often than might be inferred from inspection of Doppler velocity RHIs alone, even in cases where the billows are of large amplitude, up to 1 km in depth. Billows, and other less well-defined shear features presumably associated with billows, occur predominantly in frontal shear zones, where they may have a significant effect on the kinematic, thermodynamic and chemical properties of the atmosphere. The method described here provides a way of estimating these effects, and whether or not they have any meteorological significance.

There is a considerable contrast between the multiple shear layers observed and the way in which fronts tend to be represented in most numerical weather prediction models. For example, the Met. Office Unified Model tends to represent frontal zones as one broad shear layer. In addition, as this model parameterises mixing only in the boundary layer, frontal zones in the free atmosphere are prevented from collapse, in the presence of a deformation field, only by an implicit numerical diffusion in the vertical, rather than an explicit Richardson number dependent diffusion intended to represent mixing by KH billows, and a rather arbitrary horizontal diffusion. Although the horizontal resolution (17 km) of the mesoscale version of the model is too large to resolve KH instability, the vertical resolution is just sufficient, at least in the lower troposphere (see ahead to Fig. 4.2), to resolve the multiple layers that are observed. It is not clear whether the non-existence of these layers in the model has any significance. However, as the model's vertical resolution improves with the development of new versions of the model, some representation of mixing by KH billows will need to be represented in order to prevent the model's frontal zones from collapsing in an unrealistic manner.

CHAPTER 3

Mixing across a warm frontal zone

3.1 Introduction

This chapter describes in detail the analysis of radar data obtained during the passing of a warm front on 6 September 1995, focussing on the large-amplitude billows that are clearly visible in the Doppler data. The structure of the billows and the air flow through them is derived, showing how they mix air over a depth comparable with the depth of the frontal zone itself. This mixing is quantified to some extent by momentum flux calculations, which show how the billows strongly affect the mean velocity profiles.

3.2 Synoptic situation and nature of the data

On the evening of 6 September 1995 a surface warm front approached and passed over southern Britain (see Fig. 3.1). Between 1500 and 2240 UTC reflectivity and Doppler data were obtained concurrently within an area of light rain and drizzle using the Chilbolton radar. Most of the data were in the form of RHIs at azimuth spacings of a few degrees although some PPIs were made. The approximate location of billows is shown in Fig. 3.1(b), and the shear responsible for their generation was orientated perpendicular to this cross-section. Further details will be given in the following chapter which describes the role played by the larger, mesoscale structure of the frontal region in determining the location of the billows. It also describes the thermodynamic structure, which cannot be obtained from the radar observations.

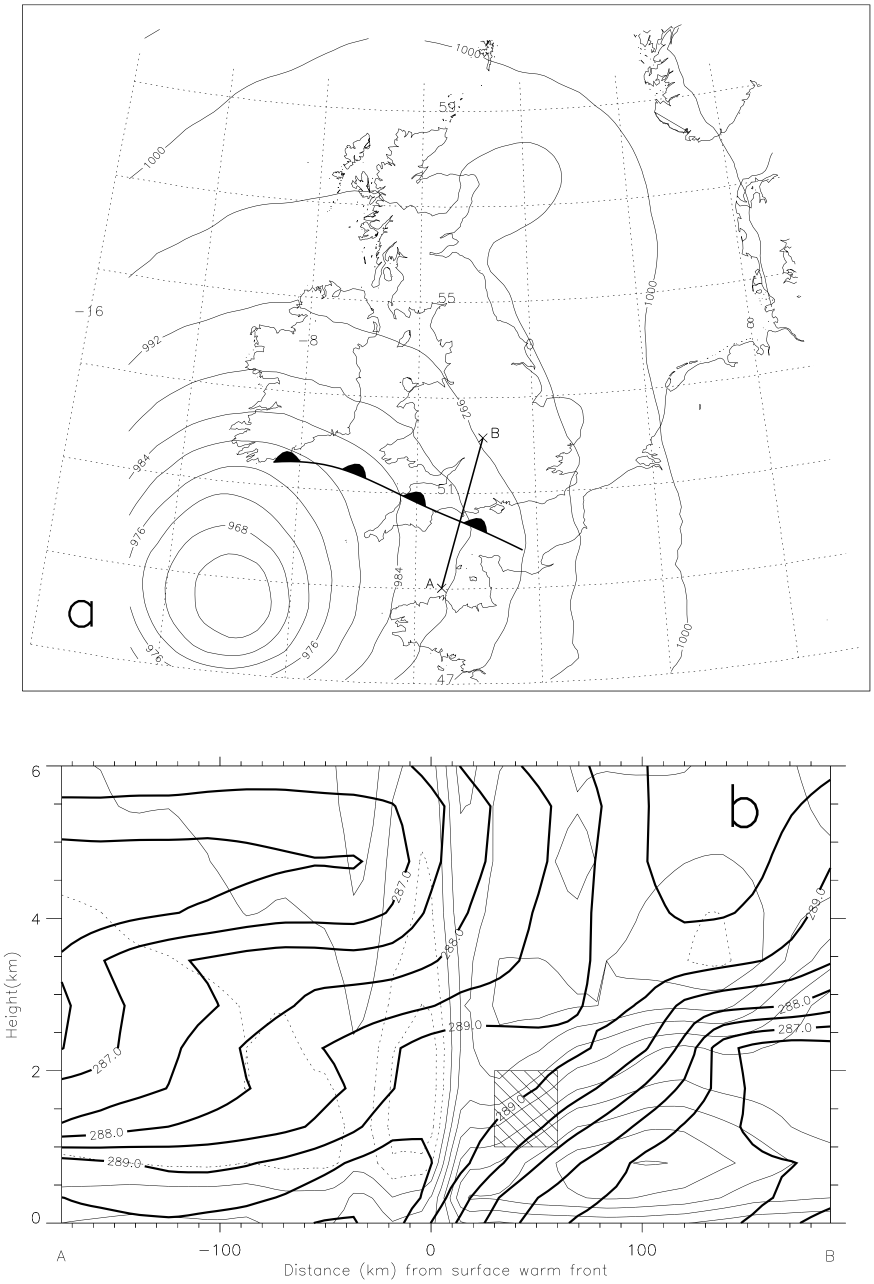

Figure 3.1: (a) Synoptic chart at 2100 UTC based on a 3 hr forecast from the UKMO Mesoscale Model showing the mean sea level pressure field (mb) and the position of the surface warm front relevant to this study. (b) Vertical cross-section along line AB in (a). Bold contours are of θ_w (K). Lighter contours show the component of wind *into* the plane of this section (intervals of 1 m s^{-1}); solid lines indicate positive values, dotted lines indicate negative values. In the study billows were observed in the region of strong shear just north of the surface warm front, as indicated in the figure.

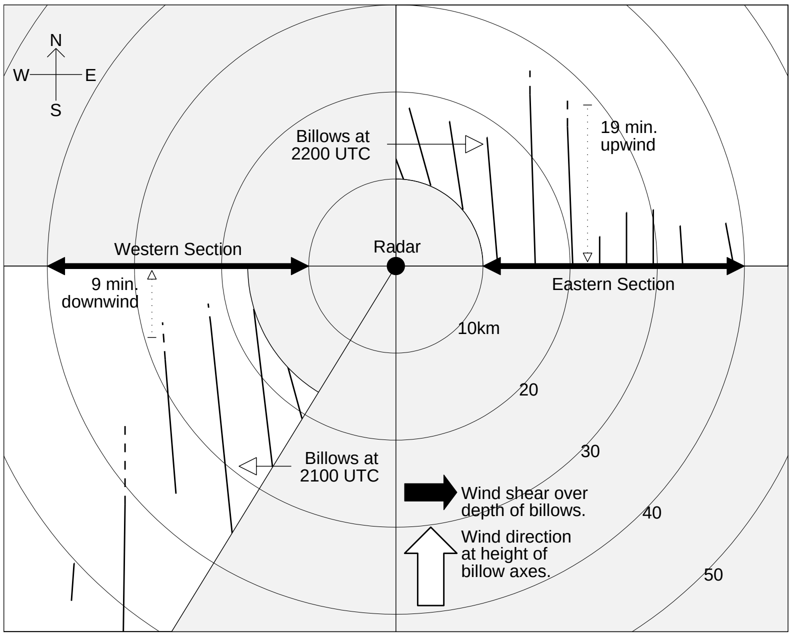

Figure 3.2: Schematic plan view showing location of billow crests (i.e. localised Doppler velocity maxima) southwest and north-east of Chilbolton Radar at times 2100 and 2200 UTC respectively. No data were available in the shaded region. Locations of vertical sections described in text and in Fig. 3.5 are shown as bold arrows labelled Western Section and Eastern Section respectively. Broad arrows at foot of diagram show that there was a strong wind component along the billow axes, at right angles to the main component of shear. Thus the billows went through their life cycle from south to north; the dotted arrows show times of the western and eastern section in relation to the northern (decaying) ends of the billows.

3.3 Observations of the billows

3.3.1 Basic observations

Figure 3.2 shows a schematic plan view of the location of billows (as determined from velocity perturbations in RHIs such as that shown later in Fig. 3.5(a)) around the radar at times 2100 and 2200 UTC. Vertical cross-sections of Doppler velocity were available in the region of the billows over two periods of time. Between 2010 (which was the time at which billows were first observed in RHIs, although they could be seen, very faintly, as early as 1930 UTC in PPIs pointing south of the radar) and 2100 UTC observations were made southwest of the radar. From 2200 until 2240 UTC observations were made north-east of the radar. Between 2100 and 2200 UTC observations were made at ranges greater than 50 km, where no billows were observed, probably

Start time of scan sequence (UTC)	Number of scans	Azimuth range	
		start	end
2007	10	268.5	211.5
2019	20	268.5	211.5
2038	10	211.5	238.5
2043	10	211.5	238.5
2050	20	211.5	268.5
2159	19	87.5	0
2210	20	90	0
2223	20	90	0
2244	18	65	-15

Table 3.1: The time and azimuth range of all RHI scan sequences showing billows in the Doppler data. Note: A sequence starting at 1954 UTC covering the same azimuth range as that at 2007 UTC displayed no evidence of billows. The sequence starting at 2244 UTC was the last made by Chilbolton radar during that observing period. Scan sequences made between 2123 UTC and 2159 UTC were made at ranges greater than 50 km (i.e. not in the same region as scans which did contain billows). Apart from this interval, the above list contains all of the scan sequences made between 2007 UTC and 2248 UTC. For clarity, times are rounded to the nearest 10 minutes when referred to in the text.

as a result of the decrease in resolution at long ranges. Further details are given in Table 3.1.

The billows had a wavelength of around 5 km when observed to the west of the radar, and around 4 km to the east. Other properties such as the amplitude and phase speed (which was less than 1 m s^{-1}) of the billows were also found to be very similar on both sides of the radar, and billows to the west of the radar are thought to have behaved in a broadly similar way to those to the east.

3.3.2 Evolution along the length of the billows

The surface warm front (as defined by sharp gradients in the wind field from CAPPIs, reconstructed from RHIs at azimuth spacings of around 10°) was moving northwards at approximately 10 m s^{-1}. The patch of billows also appeared to have a northwards component of velocity ap-

Figure 3.3: Hodograph showing wind velocity as a function of height within billows north-east of radar at 2210 UTC. Height labels in kilometres; values plotted at 0.2 km intervals.

proximately equal to this (although this could not be determined accurately), implying that the region containing billows was fixed relative to the surface front. A hodograph derived from radar data at 2210 UTC within the billows to the north-east of the radar is shown in Fig. 3.3. Two Doppler velocity RHIs were used in this calculation, one at an azimuth of 90° and the other at an azimuth of 45°. Doppler velocities from these RHIs were interpolated onto a grid which was then mapped onto a new vertical section at an azimuth of 88°, chosen to be perpendicular to the billows between 10 and 22 km east of the radar. This section thus contained wind velocity components in two directions, at 90° and 45°. These data could then be manipulated to give the wind components resolved parallel to and perpendicular to the section, as shown in Fig. 3.4. Averaging these components over two wavelengths (approximately 8 km) gave the hodograph shown in Fig. 3.3. This shows a layer of shear between 0.4 and 1.6 km in height within which there existed a strong west-east component of shear perpendicular to the billow axes. At the mean height of the billows, the hodograph shows a southerly component of wind around 20 m s^{-1}, so in a reference frame fixed relative to the front, there was a southerly wind of around 10 m s^{-1} relative to the billow patch. As the billows developed at the southern end of the patch as a result of process described in Chapter 4, they were advected northwards whilst continuing to grow. They then "broke" and decayed at the northern end of the patch. Thus successive west-east RHIs intersected the billows at different stages in their evolution as the patch moved northwards over a west-east line through the radar. The along-axis length of the billows appeared to be of the order of 30 km, which gives a lifespan of each billow of the order of 50 minutes (although the patch of billows existed for over 3 hours because of the continuous regeneration of the billows at their southern end). The zero west-east component of wind at an altitude of 1 km is consistent with the observation that the billows had a zero phase speed in this direction relative to the ground.

Figures 3.5(c)-(f) show cross-sections of the vertical shear of the westerly component of the horizontal wind, derived from Doppler RHIs in a west-east direction such as that shown in Fig. 3.5(a). Figures 3.5(a)-(d) show the active parts of the billows to the east of the radar, and Figs. 3.5(e) and (f), obtained at earlier times when the patch of billows was further south, show the shear downwind of the billows to the west of the radar.

Parts of the cross-sections of shear shown in Figs. 3.5(c)-(f) and a cross-section derived from the RHI at 2210 UTC were averaged (over approximately 14 to 24 km east of the radar in Figs. 3.5(c) and (d), and 20 to 30 km west in Figs. 3.5(e) and (f)) to generate the mean shear profiles shown in Figs. 3.6(a) and (b). The approximate location of the cross-section relative to the end of the billows that were averaged over was determined, and knowledge of the mean wind through the billows allowed the time of each profile within the lifecycle of the billows to be calculated. These varied from 19 to 25 minutes upwind of the region of collapse in Fig. 3.6(a) and from 9 to 19 minutes downwind of the region of collapse in Fig. 3.6(b). An additional profile (Fig. 3.6(c)) was derived just upstream of a billow by combining Doppler data from an earlier RHI (at 2010 UTC) at an azimuth of 211.5° with the southerly component of wind from the hodograph in Fig. 3.3, after correcting for the effects of the frontal slope. Although this profile will not in detail be accurate as there was only 30° between the wind components used to derive it, it does show that the shear layer upstream of the billows was only around 1 km thick, similar in thickness to the profiles from within billows to the north-east of the radar, and considerably thinner than in profiles from downstream of billows to the west of the radar. A schematic plan view showing the time of these profiles in relation to the billows is shown in Fig. 3.7.

The sequence of shear profiles (Figs. 3.6(a) and (b)) shows that within the billows (Fig. 3.6(a)), a single shear layer became split into two over a short period of time. Downwind of the billows (Fig. 3.6(b)) there existed a broad split shear layer (solid line), though further downwind the split was less well defined (dotted line). The greater depth of the shear layer to the west of the radar

(Fig. 3.6(b)) than to the east (Fig. 3.6(a)) is discussed in Section 3.4. The detailed evolution of the structure of the shear layer can be observed in the relevant parts of Figs. 3.5(c)-(f), and is consistent with the evolution described by Browning and Watkins (1970).

3.3.3 3D air flow through the region containing billows

Also shown in Fig. 3.5(a) is a streamfunction derived by integrating the continuity equation upwards from the ground, as described in section 2.5.1. The streamfunction is superimposed on the Doppler winds, indicating parcel trajectories projected onto the plane of the RHI (there was a mean southerly front-relative wind of 10 m s^{-1} into this plane at the level of the billows). This shows that air parcels within the billows (centred at a height of approximately 1 km) followed trajectories that were approximately helical, with the main axis aligned in a south-north direction. Integrations around closed contours indicated that the time taken for air parcels to complete a closed circuit within a billow was approximately 20 minutes, which compares well with the lifetime of 50 minutes mentioned previously. The main assumption in deriving the streamfunction was that there was no variation of the south-north component of velocity along the length of the billows. Although this assumption may be validated over the whole length of the billows, as is done in Section 3.4.2, validation is not so straightforward on smaller scales, as the billows themselves might create localised variations by advection of the south-north velocity component. However, there is clearly a strong correlation between the rolls shown by the streamfunction and the undulations in the Doppler data, indicating that the assumption was in fact valid and that the billows were essentially 2-dimensional in the region of the RHI. The same was true of a west-east RHI obtained at 2210 UTC (not shown). However, a similar manipulation of the Doppler data to give the streamfunction at 2200 UTC (also not shown) showed a weaker correlation. This may have occurred partly as a result of ground clutter, made worse by the particularly low reflectivity at ranges less than 25 km at this time, or it may have been due to a less vigourous overturning in the billows that were sampled at this time. This latter explanation is consistent with the RHI being located closer than the other RHIs to the northern end of the billows at 2200 UTC, and thus further advanced in the lifecycle (Fig. 3.7).

Figure 3.5(b) shows the vertical velocity (with the streamfunction from Fig. 3.5(a) superimposed) which was obtained from the Doppler velocity with the same 2-dimensional assumption that was used to derive the streamfunction. It can be seen that the billows induced vertical velocities locally as large as $\pm$ 3 m s^{-1}.

3.4 The effect of the billows on the mesoscale frontal structure

3.4.1 Introduction

The Doppler radar wind profiles within and downwind of the billows showed a considerable change over a south-north distance of around 30 km (see Figs. 3.6). Part of this change was due to the lifting of the overall frontal shear layer with distance ahead of the surface front. The other part of the change was due to the shear over the layer containing billows being redistributed over a greater depth. Although the nature of the latter part of the change is consistent with it having been caused by the billows, it could alternatively be a feature of the larger-scale flow field. In Section 3.4.2, estimates are presented of the vertical profiles of the vertical flux of horizontal momentum due to the resolvable flow patterns associated with the large-amplitude billows. Although the estimates are prone to considerable error and do not constitute an adequate statistical sample, they tend to support the view that the billows themselves could have been responsible for the observed change in the wind profile over their length.

3.4.2 Calculation of momentum flux from radar measurements

The Reynolds decomposition for data from point measurements is performed by separating fields into their time-mean and time-dependent parts, such that the time scales of the two parts are widely separated. However, in the present case, the data are in the form of spatial fields of the front-parallel (i.e., west-east) component of the wind and so the measurements are separated instead into their horizontal-mean and horizontal-dependent parts

$$u = < u > + u^* \qquad\qquad w = < w > + w^*$$

where the mean is taken over an integral number of billow wavelengths. The axes used here are orientated so that the x-, y- and z-axes point east, north and upwards, respectively. The 2D circulation through the billows lies, rather conveniently, in the x, z plane. Observations showed that the billows had a west-east phase speed of less than around 1 m s^{-1}, so the x-axis is essentially fixed relative to the ground. The y-axis is taken as moving northwards at 10 m s^{-1}, the northwards speed of the front and billows, so that there was effectively no time evolution in the reference frame used. The effect of the billows on the mean u profile may be obtained in the following manner.

The following properties of the averaging procedure may be easily obtained (for example, see Stull 1988):

- The average of a mean quantity in the x-direction is the mean quantity itself, i.e.

$$<< u >>=< u > . \tag{3.1}$$

- The average of a perturbation quantity in the x-direction is zero, i.e.

$$< u^* >= 0. \tag{3.2}$$

- The gradient in the x-direction of a mean quantity is zero, i.e.

$$\partial < u > /\partial x = 0. \tag{3.3}$$

- The average of a gradient quantity (both taken in the x-direction) is zero, i.e.

$$< \partial u^*/\partial x >= 0. \tag{3.4}$$

The terms in the x-component of the momentum equation may be expanded to give

$$(< u > +u^*)\frac{\partial(< u > +u^*)}{\partial x} + (< v > +v^*)\frac{\partial(< u > +u^*)}{\partial y}$$

$$+(<w>+w^*)\frac{\partial(<u>+u^*)}{\partial z}=f<v>-\frac{1}{\rho}\frac{\partial(<p>+p_{ls}+p^*)}{\partial x} \qquad (3.5)$$

where $\partial p_{ls}/\partial x$ represents the large-scale pressure gradient in the x-direction, henceforth assumed to be in balance with the term $f<v>$. The mean vertical velocity is taken as zero. The terms $\partial<u>/\partial x$ and $\partial<p>/\partial x$ are both zero according to (3.3). Expanding (3.5) and removing those terms which are zero for the reasons just mentioned gives

$$<u>\frac{\partial u^*}{\partial x}+u^*\frac{\partial u^*}{\partial x}+<v>\frac{\partial<u>}{\partial y}+<v>\frac{\partial u^*}{\partial y}+v^*\frac{\partial<u>}{\partial y}+v^*\frac{\partial u^*}{\partial y}$$
$$+w^*\frac{\partial<u>}{\partial z}+w^*\frac{\partial u^*}{\partial z}=\frac{1}{\rho}\frac{\partial p^*}{\partial x}. \qquad (3.6)$$

This may then be averaged over in the x-direction, to give an expression containing the gradient of $<u>$ in the y-direction

$$<u^*\frac{\partial u^*}{\partial x}>+<v>\frac{\partial<u>}{\partial y}+<v><\frac{\partial u^*}{\partial y}>+<v^*\frac{\partial u^*}{\partial y}>+<w^*\frac{\partial u^*}{\partial z}>=0 \qquad (3.7)$$

after removing terms which are zero because of (3.4) and (3.2). The third in term in (3.7) is also zero according to (3.2) as it is equal to $<v>\partial<u^*>/\partial y$. Equation (3.7) may be put into flux form by making use of the continuity equation[1] (which the perturbation quantities must satisfy), after multiplying it by u^* and averaging to give

$$<u^*\frac{\partial u^*}{\partial x}>+<u^*\frac{\partial v^*}{\partial y}>+<u^*\frac{\partial w^*}{\partial z}>=0.$$

Adding this to (3.7) gives

$$<v>\frac{\partial<u>}{\partial y}+<\frac{\partial u^*u^*}{\partial x}>+<\frac{\partial u^*v^*}{\partial y}>+<\frac{\partial u^*w^*}{\partial z}>=0$$

after combining pairs of terms. The second term is identically zero as it is an average of $\partial/\partial x$ quantity. Ultimately, we will be interested in profiles averaged over the whole lifecycle of the

[1] The absence of the vertical derivative of the background density in the continuity and momentum equation is a reasonable approximation because the vertical scales of motion are small compared to the density scale height.

billows, so the gradient in the y-direction in the third term means that it will eventually become zero. In any case, Fig. 3.4 showed that the billows had little effect on the component of wind in the y-direction, so terms involving v^* should be negligible even for individual profiles. Removing these terms which are either zero or very small gives

$$< v > \frac{\partial < u >}{\partial y} = -\frac{\partial < u^* w^* >}{\partial z}, \tag{3.8}$$

where $< v >$ is equal to 10 m s^{-1}, the southerly component of the wind relative to the front at the height of the billows. Equation (3.8) relates the change in the west-east component of the wind to quantities which may be measured by the radar, as will be demonstrated.

Intuitively, it might be thought that the assumption of two-dimensional flow in the derivation of the vertical velocity is inconsistent with the observed and expected variation in the along-axis direction. However, the assumption made is that $\partial v/\partial y$ is much smaller than $\partial u/\partial x$. Even if the billows induced a change in v of as much as 5 m s^{-1}over the length of the billows (40 km), i.e. an along-axis divergence of order 10^{-4} s^{-1}, this is small compared to the divergence in the plane of the billows, which was around 10^{-3} s^{-1}. Therefore the assumption made seems to be reasonable.

At 2210 UTC four billows which existed due east of the radar were sampled. A plan view of these billows ten minutes earlier can be seen in Fig. 3.2. They were chosen because of their proximity to the radar, and lack of ground clutter in the radar data, although the billow closest to the radar could not be used because of the limited vertical extent of the RHI at short range. The four billows will be referred to as I, II, III and IV, from west to east. The Doppler velocity in this direction gives u directly, and this was interpolated onto a regular grid with spacing 500 m in the horizontal and 100 m in the vertical. This spacing was chosen to correspond broadly to the spatial resolution of the radar data over the ranges used. The vertical velocity, w was calculated as has been described previously, using a nine-point average around each grid box to smooth the u field. The quantities $< u >$ and $< w >$, taken as averages of u and w over the four billows between $x = 13.5$ and $x = 31.5$ km, and values of u^* and w^*, were calculated accordingly.

Figure 3.8 shows the $x - z$ cross-sections of (a) u^* and (b) w^* which were then combined to give (c) $u^* w^*$. The four billows all show the same qualitative structure in each of these fields.

Although u^* and w^* vary with the same wavelength as the billows, the field of u^*w^* varies in the horizontal with a wavelength half that of the billow wavelength. For example, over billow IV between 27 and 31.5 km at a height of 1 km, u^*w^* shows a maximum, minimum, maximum then a minimum. There is a further set of maxima and minima at a height of 1.7 km, out of phase with those below. This is consistent with Fig. 13 of Busak and Brümmer (1987) who used a linear analytical model to simulate billows close to the ground. The u^*w^* field was averaged horizontally over each individual billow to give the four mean momentum flux profiles in Fig. 3.9. As might be expected from Fig. 3.8(c), profiles from billows I and II are similar to each other, as are profiles from III and IV. However, the latter pair have larger maxima and minima over the depth of the billows, and there is also a displacement in the vertical between the two pairs of profiles, such that the two pairs are approximately in anti-phase with each other. Good quality Doppler data were also available over two other billows (not shown); the momentum flux profiles from these are qualitatively similar to the profiles from I and II.

Only two-dimensional eddies on horizontal scales between around 0.5 and 4 km can contribute to the momentum flux profiles calculated in this way, due to the resolution of the radar data and the way the vertical velocity is calculated. Thus it is only the effect of the main overturning of the billow on the mean velocity profile that is being measured, not the effect of its turbulent breakdown by eddies on smaller horizontal scales.

It is likely that a billow going through different stages of evolution would have different momentum flux profiles at each stage, which would account for some of the variation between the flux profiles in Fig. 3.9. This is supported by the numerical simulations by Fritts *et al.* (1996a), which show that the momentum flux is strongest as the billows grow to maximum amplitude, but then fluctuates with time, even reversing in sign, before it decays to zero. In order to obtain an estimate of the net change in the mean wind profile from upstream to downstream of the billows, all six available momentum flux profiles were averaged. Although it was hoped thereby to sample the billows at six different stages in their evolution, it is not known how well they represent all stages in the evolution and so we have rather low confidence in the representivity of the average profile. The resulting profile is shown in Fig. 3.10(a), together with a smoothed profile. Smoothing was carried out so that small-scale fluctuations did not dominate in the derivation of the first and second vertical derivatives, as discussed in the following section.

3.4.3 The effect of the momentum flux convergence on the mean wind shear profile

According to (3.8), the rate of change of the mean wind following the flow is given by the momentum flux convergence. Similarly, the rate of change of the mean wind shear following the flow is given by the vertical derivative of the momentum flux convergence. Averaged profiles of these two quantities, derived from Fig. 3.10(a), are plotted in Figs. 3.10(b) and 3.10(c), respectively. Equation (3.8) has been used to estimate the change in shear profile between locations 5 km south and 5 km north (solid and dashed curves, respectively, in Fig. 3.11(a)) of the original location of the profile. The shear responsible for the billows initially had a maximum at a height of 1.1 km, and was zero at 1.5 km. At 1.1 km, the vertical derivative of the momentum flux convergence was negative, indicating a tendency for the billows to reduce the peak shear at this height (see arrow in Fig. 3.11(a)). Between 1.3 and 1.8 km the vertical derivative of the momentum flux convergence was positive, indicating a tendency for the billows to increase the shear, thereby spreading the shear layer out over a greater depth in the vertical. The effect on the shear at lower levels (below 0.5 km) appears to have been considerably less.

3.4.4 Comparison of calculated and observed profiles of wind shear upwind and downwind of the billows

The observed profiles of wind shear at locations towards the southern end and downwind of the billows separated by a distance of around 30 km are shown in Fig. 3.11(b). This separation is greater than that used above because of the interval between times when scans could be observed, as mentioned in Section 2(b). The trends in these profiles are in broad agreement with the trends in profiles inferred from momentum flux calculations, showing a decrease in peak shear, but an increase in shear above 1.4 km, and a smaller increase below 0.6 km. However, these results should be treated with caution, as there are a number of important sources of error:

- The calculation of w is susceptible to inaccuracy in two ways. Firstly the assumption of non-divergence in the south-north direction may induce a systematic bias in the vertical velocity if this component of divergence is itself influenced by the billows. The nature of the radar data make it impossible to estimate the magnitude of this effect, although the variation of the south-north component of divergence in the west-east direction is unlikely to have been comparable to the west-east component of divergence itself. Secondly, the vertical velocity field was obtained by integrating upwards from as close to the ground as possible. However, at low levels the radar beam is contaminated by echos from the ground itself, so the level at which the integration was started (200 m) was relatively high, considering the low altitude of the billows. The effect of errors in w near the ground amplify with height, making this a potentially serious problem. The fields of w obtained are to a large extent validated only by qualitative comparison of the streamfunction with the original wind field. However, they do agree well with the prediction by Davis and Peltier (1976) that the maximum in the vertical velocity can occur higher than the critical level for the fastest growing instability when the shear layer is close to the ground. Also, if the vertical velocities in each column are adjusted by including a constant divergence at all levels in the column sufficient to produce zero vertical velocity at a height of, say, 3 km (at which height the Doppler velocity and wind shear perturbations are relatively small, implying that this is a reasonable upper boundary condition), the momentum flux calculations give essentially the same result. Unfortunately this procedure can only be performed for a few of the billows, as for many no data were available at sufficiently high levels.

- The vertical velocity calculated represents only the main overturning of the billows, not the small-scale eddies involved in its turbulent breakdown. It is not obvious *a priori* which scale contributes most to the deepening of the shear layer, and how the contribution of each scale varies over the lifetime of the billows. However, three-dimensional numerical simulations by Fritts *et al.* (1996a) indicate that it is mainly the overturning of the billow that affects the mean velocity profile, rather than smaller scale eddies associated with the breakdown of the billow, although these eddies influence the mean profiles indirectly via the evolution of the billow itself. This suggests that the method used here should, in principle, allow measurement of the momentum fluxes responsible for the change in mean shear profile over the lifecycle of billows.

- The sample of six billows is too small to show whether the variation seen in the individual momentum flux profiles is due to variation in the actual billow structure, or due to random errors. Even if the former were true, the sample size would still be too small for a reliable estimate of a representative average momentum flux profile over the lifetime of the billows.

As it happened, the measurements available were through billows that were overturning strongly, probably towards the middle of their lifecycle, so the results support the view that the overturning of the billows may indeed have been responsible for a large part of the observed change in wind shear profile over the length of the billows. The limitations of the present dataset are such that the closeness of the agreement between the momentum flux calculations and the profile changes up and downwind of the billows is probably very fortuitous. The calculations have been done in a way that is analogous to the analysis of data from tower (e.g. Blumen 1984) and aircraft (e.g. Metcalf and Atlas 1973, Busak and Brümmer 1987) measurements, i.e. by making averages of correlations over many billows, with no attempt to obtain multiple measurements over an individual billow's lifetime. Any estimate of the momentum flux variance will therefore include the variation of u^*w^* within a billow as well as random errors and variation in the momentum flux profile over the lifetime of the billows (as shown by Fritts *et al.* 1996a). It is therefore in general very difficult to estimate the uncertainties associated with measurements of momentum fluxes, and studies frequently do not even attempt such an estimate.

Given a dataset that had been acquired specifically in order to obtain momentum flux estimates over the lifetime of a train of billows, there are two ways in which errors associated with the momentum flux profiles could be estimated:

- Radar RHIs provide a way of obtaining measurements over a train of billows at intervals of as little as 20 seconds. This is sufficiently short a period (relative to the time-scale for the evolution of a billow) that consecutive momentum flux profiles, calculated over an individual billow, should change very little and certainly remain qualitatively similar. If this were not the case, it would indicate that the assumptions used in the derivation were not valid. On the other hand, a number of consecutive momentum flux profiles, obtained over a time significantly less than the time-scale for the evolution of the billow, would allow a quantitative estimation of the random errors associated with each individual profile. Errors associated with, for example, *localised* departure from 2D flow would, in effect, be random in this context, so their effect on the final profile could be estimated using statistical methods.

- Given validation of the general method as outlined above, individual momentum flux profiles from a single billow could be averaged to obtain a single profile representative of the mixing by that billow over its whole lifetime. This would be possible only if the billow was not advected out of the range of the radar in the time taken for the billow to pass over the radar. Profiles obtained in this way through a number of billows could then be averaged, and an error estimate could be obtained by taking the standard deviation of $< u^{*}w^{*} >$ at each height. It is clearly not possible to do this with the existing dataset, given its limitations which have already been described.

3.5 Reflectivity structures associated with the billows

Figure 3.12 shows a PPI of reflectivity at an elevation of 0.5° over the NE sector obtained just prior to the NE sector RHI scans analysed in the previous sections. Although the minimum range in this scan was 50 km, it does show that a banded structure existed orientated approximately in a S-N direction (note that the nature of PPIs means that orientations are distorted, as the beam altitude increases with range). These bands had a horizontal (W-E) length scale of around 10 km, though no clearly defined wavelength, so could not have been occuring in a fixed position relative to the billows. The reflectivity bands were also visible in RHIs over the sector between 2200 and 2220 UTC , appearing as arc-shaped reflectivity cores of up to 30 dBZ, corresponding to rain rates of between 3–4 mm hr^{-2} if estimated using the Z-R relationships given in the Introduction. The reflectivity cores occurred within a fairly uniform background reflectivity of less than around 2 dBZ. The locations of these cores for a sequence of RHIs has been plotted in Fig. 3.13 to indicate the bands' orientation and location. This section shows how they relate to the air flow through the billows, and thus the larger scale frontal structure.

The three W-E reflectivity RHIs available in the NE sector are shown in Fig. 3.14, with vertical velocities from a streamline calculation superimposed. There does appear to be some correlation between the core locations and the vertical velocity maxima, with the latter tending to occur in the weak reflectivity regions just to the west of the cores. However, the strength of this association varies considerably from one billows and time to the next. There are also cores which are not apparently associated with billows, but according to Fig. 3.13 occur in S-N lines.

One possible explanation for the reflectivity cores not being closely related to the vertical velocity maxima within the billows is that the updrafts within and, to a certain extent, above the western part of each billows, induce condensation and the formation of convective cells in the potentially unstable layer just above the height of the billows. These cells would then travel with the mean wind (i.e. to the NE relative to the air within the billows, perhaps explaining the tendency of the bands in Fig. 3.12 to be orientated with their axes along an azimuth of around 30°) at their height of around 2–3 km. Such convective cells can be seen in time-sequences of FRONTIERS data. As a result, any phase relationship with the billows would be lost. A schematic diagram showing how the reflectivity cores may have been formed is shown in Fig. 3.15. The stages labelled A-D are as follows:

- At A: Initially, a saturated parcel is lifted by the updraft in a billows, inducing condensation and growth of droplets that are sufficiently small in size to be carried with the air. The height of the melting layer (just visible at a range of 25–30 km in Fig. 3.14(a), but more clearly visible in Zdr RHIs) was 2.8 km, so these droplets remain liquid in all the processes considered here.

- Between A and B: The droplets coalesce, forming a smaller number of larger droplets, which eventually become sufficiently large to fall through any updraft. Alternatively, droplets may reach B from convective cells in the potentially unstable region just above A.

- Between B and C: The droplets continue to grow by coalescence and collection of droplets from the saturated air through which they are falling (e.g. Wallace and Hobbs 1977). Although the liquid water content will not change much following the droplets, as the reflectivity is proportional to D^6, it increases rapidly. Their trajectory is determined mainly by the horizontal wind, which is sheared, as the vertical velocity in this part of the billow is small. This is described in more detail below.

- Between C and D the droplets are falling through unsaturated air (as shown in Chapter 4). As evaporation will affect the largest droplets less than the smaller ones, the reflectivity decreases only slightly with decreasing height.

If the forcing and supply of water at A is approximately constant on a time-scale of 5–10 minutes (the time taken for droplets to fall 1.5–2 km at a velocity of 4 m s^{-1}), the above process will give rise to an arc-shaped reflectivity pattern consistent with that observed. Variations on longer time-scales explain the variation in the strength of the reflectivity cores between the RHIs.

Relationships between reflectivity and rain-rate, as mentioned in the introduction, rely on the drop-size distribution having an exponential form. This may be the case if the distribution occurs as the result of a balance between droplet growth by coalescence and breakup as the droplets grow sufficiently large. However, in the present case the low reflectivity values indicate that the droplets remained too small for breakup to be appreciable, so a mono-dispersed distribution is likely to be more applicable. Making this assumption, and using the reflectivity and droplet trajectories (derived from the shape of the reflectivity core), allows an estimation of the precipitation rate, as described below.

Although many of the reflectivity cores were quite weak and transient, a particularly intense, clearly defined core was associated with the billows at a range of around 29 km (Fig. 3.14). At all three times, the slope in the lower half of the billows, at a height of around 500 m, was close to 45 °. As the reflectivity core appeared to be stationary relative to the billows (and thus the radar), the arc-shaped maxima in the core may be taken as indicative of the trajectories of droplets falling through it. Given a horizontal wind speed of 6 m s $^{-1}$ at a height of 500 m relative to the speed of the convective generating cell, the slope of the reflectivity core implies a vertical droplet fall-speed of 6 m s^{-1} relative to the ground. In fact, as the core was situated between the vertical air velocity maxima, this fall speed was also approximately 6 m s^{-1} relative to the air.

Using the relation $V_t = 8 \times 10^3 r$ for $0.24 < V_t < 8$ where V_t is the terminal velocity (6 m s^{-1}) and r the radius of a droplet (Young 1993) gives $r = 875\mu$m. For a mono-dispersed raindrop size distribution, the liquid water content (L) may be related to the reflectivity, drop radius and number density (N) by:

$$Z = 64Nr^6 \qquad \text{and} \qquad L = \frac{4}{3}N\pi r^3 \rho_{water}$$

giving

$$L = \frac{\pi \rho_{water} Z}{48r^3}.$$

At 2210 UTC the reflectivity was at its maximum of 1000 mm^6 m^{-3} (30 dBZ) giving $L = 10^{-4}$kg m^{-3} $= 0.1$ g m^{-3}. The rain rate is given by $LV_t = 5.9 \times 10^{-4}$ kg m^{-2} s^{-1} $= 2.2$ mm hr^{-1}, with an error of up to around 50% due to the problems and assumptions associated with obtaining the terminal velocity from the slope of the reflectivity core. This rain-rate corresponds to light rain/heavy drizzle that is slightly weaker than that obtained using the Z-R relationship above. In addition, evaporation below this level meant that the rain-rate experienced at ground level would have been even little less than this.

The liquid water content may be compared directly with the quantity of water that would be produced by lifting a layer of saturated air, say, 250 m (i.e. from A to B in Fig. 3.15). This gives around 0.3 g m^{-3}, which is consistent with the value given above, as in reality conversion of condensation into rain droplets may not have been 100% efficient. This suggests that the process described could be capable of generating reflectivity cores with the observed strength.

The hodograph (Fig. 3.3) and Doppler RHIs (Fig. 3.5) show that a westerly wind of around 6 m s^{-1} existed above the shear layer containing billows. Thus any convective cells would have moved eastwards, continuing to produce precipitation, after being initiated by the updrafts within the billows. This is a possible explanation for the reflectivity lines and cores in Figs. 3.13, 3.12 and 3.14.

Although the potential instability that existed above the billows would have been released in any case after further lifting as the air ascended over the frontal zone, the existence of billows may have caused earlier release of the instability and hence precipitation to occur further south and with a less uniform distribution than would have occurred in the absence of billows. This in turn may have had some effect on the location and vertical extent of the billows by moistening the boundary layer air that was being over-run by the front. This boundary layer air would then enter into the frontal zone and form part of the air which entered the region containing billows, as will be shown in Chapter 4.

3.6 Discussion

Many observations of KH billows in the atmosphere have been made previously using radar to detect clear-air echoes from regions of high refractive index variance occurring at airmass boundaries (Hicks and Angell 1968, Atlas *et al.* 1970, Browning and Watkins 1970, Browning 1971, Hardy *et al.* 1973). The distributions of reflectivity (and thus by implication the thermal stratification) obtained from clear-air echoes from billows are qualitatively similar to the distribution of shear shown in Figs. 3.5(c) and (d), indicating that in the present study momentum was effectively mixed in the same way as the stratification in other studies, at least to a first approximation.

The evolution of the shear layer in this case also resembles the evolution of the thermal stratification within billows of similar dimensions deduced from clear-air radar data by Browning and Watkins (1970). However, a difference is that they observed the stratification to become split into two long-lived layers downwind of the billows whereas the split shear was short-lived in the present case. The proximity of the frontal zone to the ground makes this case significantly different. It seems likely that the strong south-north component of shear due to the boundary layer (Fig. 3.3) prevented a long-lived split from being sustained within the frontal zone, although Browning and Watkins (1970) also observed no split in radiosonde profiles of the shear even though there the stratification remained split for over two hours after a mid-tropospheric billow event. In view of the proximity of the boundary layer and the curvature in the hodograph it is perhaps surprising that such well-formed billows were able to develop at all. Despite the south-north component of shear penetrating into the lower parts of the billows themselves, they had a lifespan of around 50 minutes, compared to a lifespan of around 15 minutes found by Browning and Watkins when there was no such potentially disruptive shear at the boundaries of the billows. The presence of the ground may have contributed to this long lifetime in another way as well. Davis and Peltier (1976) found that the linear growth rate of disturbances was significantly reduced as the height of the inflection point approached the shear layer half-depth. If this result has some applicability in the non-linear stage, then the evolution of the billows might be expected to proceed more slowly than an equivalent layer away from the boundary. An alternative explanation, relating the lifetime to the Richardson number, is given in Chapter 4.

Numerical models (Scinocca 1995, Sykes and Lewellen 1982, Klaasen and Peltier 1985b) and laboratory observations (e.g. Thorpe 1985) of KH billows have shown that their breakdown (under idealised conditions) may be caused by convective instability forming vortices orientated perpendicular to the billows. Whilst the billows are still growing this instability is suppressed and they remain essentially 2-dimensional. Once the billows have reached their maximum amplitude the convective instability is allowed to grow, and the billows start to attain a 3-dimensional structure. The previously noted weakness of the vortices as determined by the streamfunction calculation for the RHI at 2200 UTC (corresponding to the section within the billows closest to their northern end) may to be partly due to the onset of this 3-dimensional structure, or to the onset of less organised 3-dimensional turbulence as the convectively unstable regions cause the wave to 'break'.

KH billows have been shown to be an important cause of clear-air turbulence (CAT) (Browning *et al.* 1970b), so at any altitude KH billows as strong as these could constitute an aviation hazard. However, in this case the hazard is greatly increased due to the concentration of the moderate mean shear into regions of strong shear (up to around 25 m s^{-1} km^{-1} in this case) extending down to a few hundred metres above the ground. This would be most relevant during aircraft take-off and landing when the effects of the billows could lead to substantial localised under-estimation of the low-altitude wind shear, even at airports where wind-profilers were in use.

There are few published observations of large-amplitude KH billows in the atmosphere, and even fewer measurements of momentum flux profiles through them. Although the magnitude of the momentum flux will depend on a variety of factors, including the billow size, shear and stage in evolution, it is still worthwhile to compare the results presented in this thesis with those from other studies. In one such study Bryant and Browning (1975) used Doppler radar to investigate billows occurring at heights between 1 and 3 km within a warm frontal zone. They used very different methods from those described here to estimate the vertical flux of horizontal momentum. Whereas the billows in the present study had a wavelength of 4 to 5 km, those in the earlier study had a wavelength of 1 to 2 km. The peak shear was about the same in both studies. The magnitude of the resolved momentum flux had a maximum of around 0.1 $m^2\ s^{-2}$ in the shear layer, compared with 0.5 $m^2\ s^{-2}$ estimated here. This difference is what might be expected in view of the larger wavelength of the billows observed in the present study.

In another study of KH billows, Blumen (1984) used wind and temperature measurements from an instrumented tower to calculate turbulent momentum fluxes due to billows in two occasions of night-time drainage winds. During periods when billows existed and the wind shear profile was observed to become smoothed with time, then the momentum fluxes acted in such a way as to cause this smoothing. The fluxes had a maximum of around 0.2 $m^2\ s^{-2}$ which is less than those calculated here. Again, this would be consistent with the smaller wavelengths (100–200 m) observed by Blumen, although the shear in his case was considerably larger than here. Other measurements from instrumented towers of momentum fluxes through KH billows in the boundary layer include those by Merrill (1977), whose measurements, showing a divergence in the momentum flux (which had a magnitude of around 0.1 $m^2\ s^{-2}$) near a critical level, were shown to be consistent with predictions by a linear stability analysis.

The momentum fluxes estimated in the present study are of a similar magnitude to those observed in CAT at upper levels. For example, Kennedy and Shapiro (1979) found that the magnitude of the momentum flux within a number of upper-level turbulence zones was between around 0 and 4 $m^2\ s^{-2}$. Trout and Panofsky (1969) used clear-air turbulence spectra and clear-air turbulence probabilities (based on commercial aircraft reports) to show that the dissipation of kinetic energy by CAT between 25,000 and 40,000 ft is around 1 watt m^{-2}, which is not unimportant in the dynamics of the local atmospheric circulation.

Frequently, published analyses of radar observations have restricted themselves to obtaining basic parameters such as the wavelength and extent of the billows. Using the vertical velocity field obtained by integrating the continuity equation to obtain momentum flux measurements has not, to our knowledge, been done before. However, in spite of the consistency of the results obtained here with observations of the change in mean wind profiles and other published observations, the uncertainty in the measurement errors and the small sample size used means that the results should be treated mainly as an indication that the method used may have potential to be useful in a future case.

Figure 3.4: RHIs showing velocity components parallel to and perpendicular to an azimuth of 88°, derived from Doppler radar data at 2210 UTC from within billows which were aligned in a direction perpendicular to this azimuth.

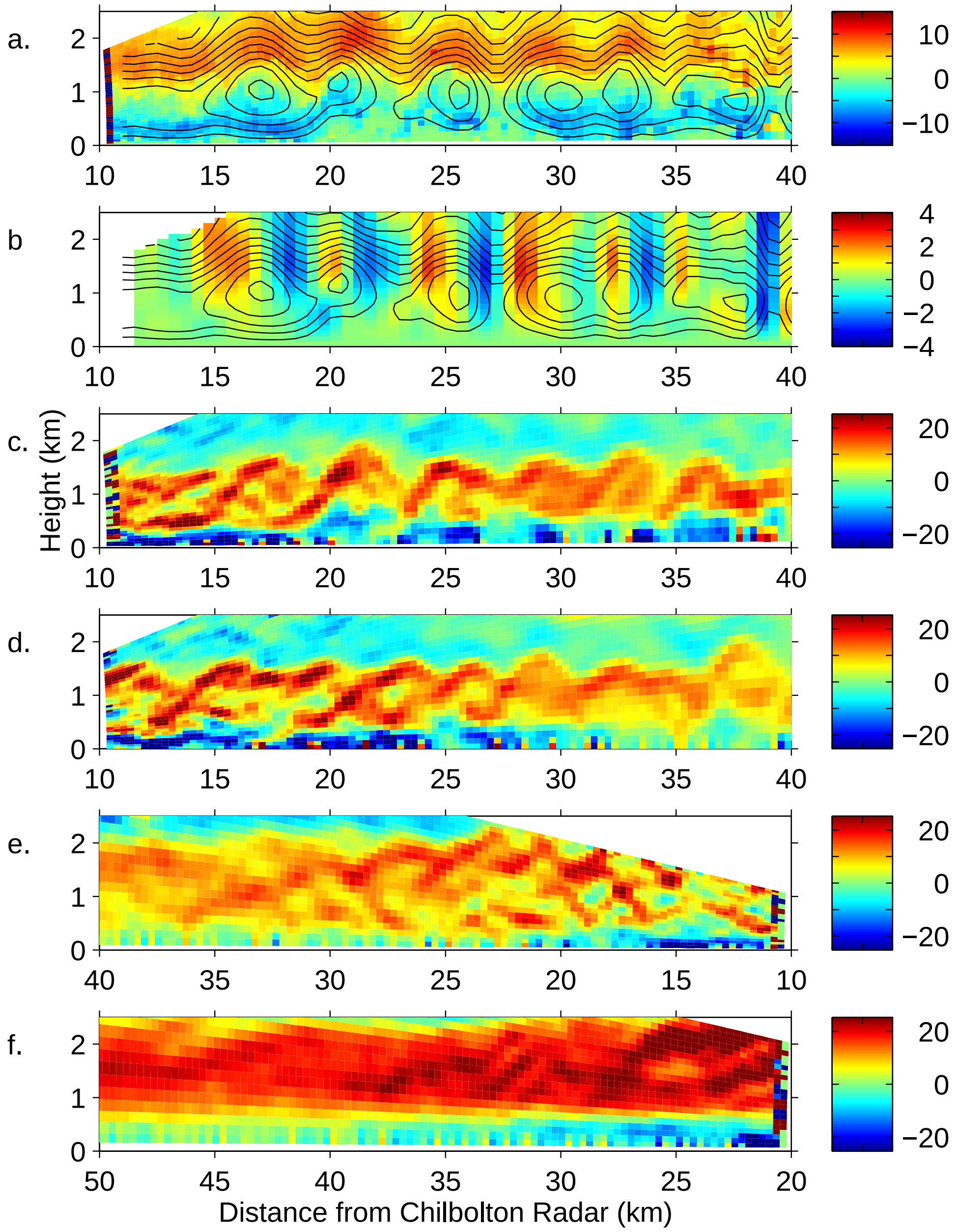

Figure 3.5: (a) Vertical west-east cross section (RHI) of Doppler velocity, effectively giving westerly wind components (m s^{-1}, blue to the left and red toward the right) at 2220 UTC. Superimposed are contours of a mass-streamfunction (intervals of 1000 kg m^{-1} s^{-1}) projected onto the plane of the RHI. (b) As (a), except shading shows vertical velocity (m s^{-1}) at 2220 UTC. (c)-(f) Vertical west-east cross-sections of shear (m s^{-1} km^{-1}) derived from Doppler velocity RHIs at times 2220, 2200, 2100 and 2020 UTC respectively. (a)-(d) are eastern sections obtained upwind, and (e) and (f) are western sections obtained downwind of the region of billow collapse.

Figure 3.6: Profiles of shear (m s^{-1} km^{-1}) averaged horizontally approximately (a) 25, 22 and 19 minutes upwind and (b) 9 and 19 minutes downwind of the collapse of the billows. These profiles are derived from averages of shear cross-sections at times 2220, 2210, 2200, 2100 and 2020 UTC, respectively. (c) is a shear profile calculated by combining Doppler data at 2010 UTC at an azimuth of 211.5° with the southerly wind component from the hodograph in Fig. 3.3.

Figure 3.7: Schematic plan view of billows (in a reference frame moving with the region containing billows) showing the locations of the RHIs from which the profiles of shear were derived, together with the times of these profiles within the billow lifecycle relative to the collapse of the billows. Negative times (up to 50 minutes) are within the billows, and positive times are downstream of the billows. The dotted line indicates the location of the "additional" profile shown in Fig. 3.6.

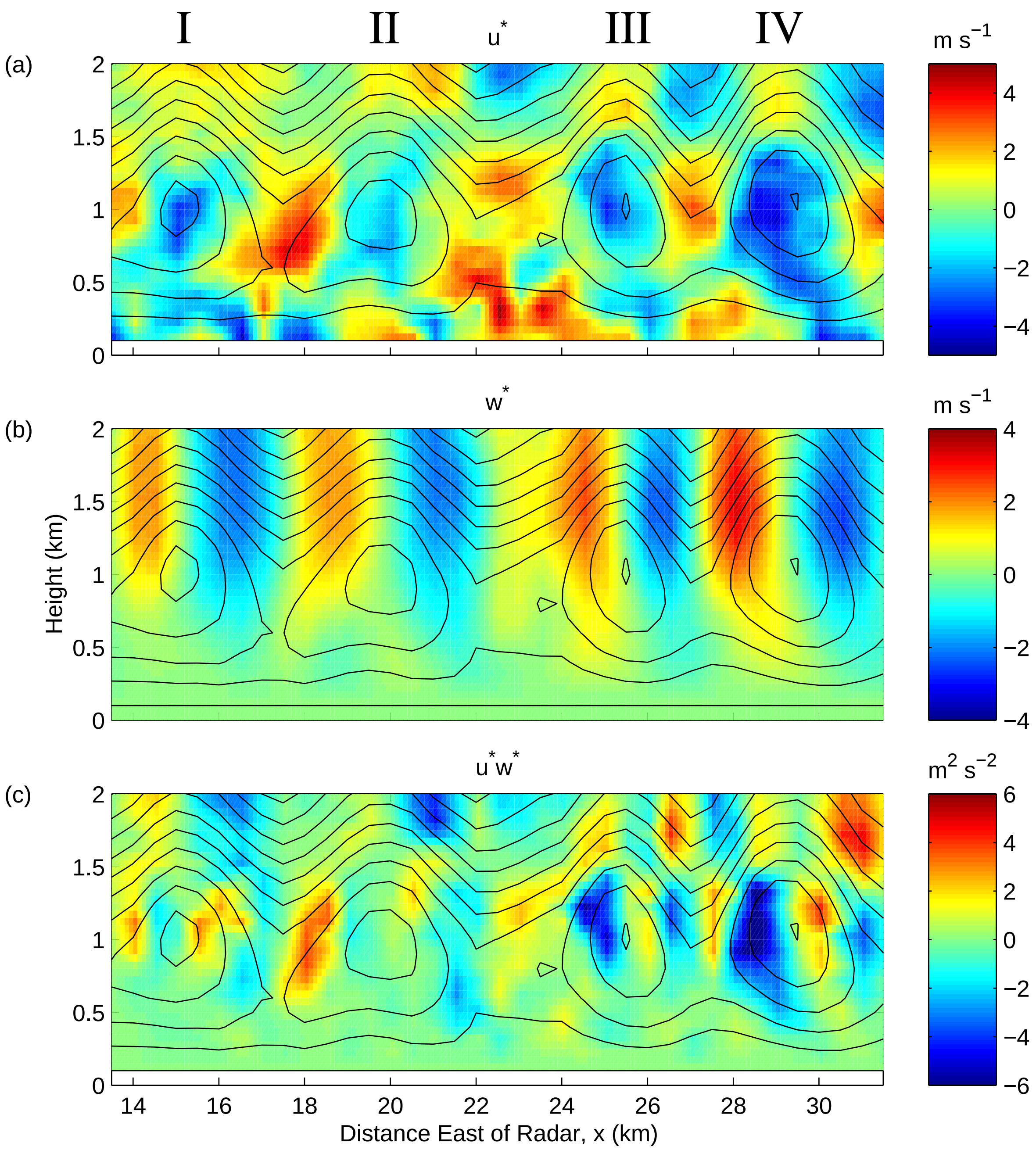

Figure 3.8: Radar-derived cross-sections through billows east of the radar at 2210 UTC, 6 September 1995, showing streamfunction (light solid contours) superimposed upon (a) u^* (m s^{-1}) (b) w^* (m s^{-1}) and (c) u^*w^* (m^2 s^{-2}). Roman numerals refer to individual billows.

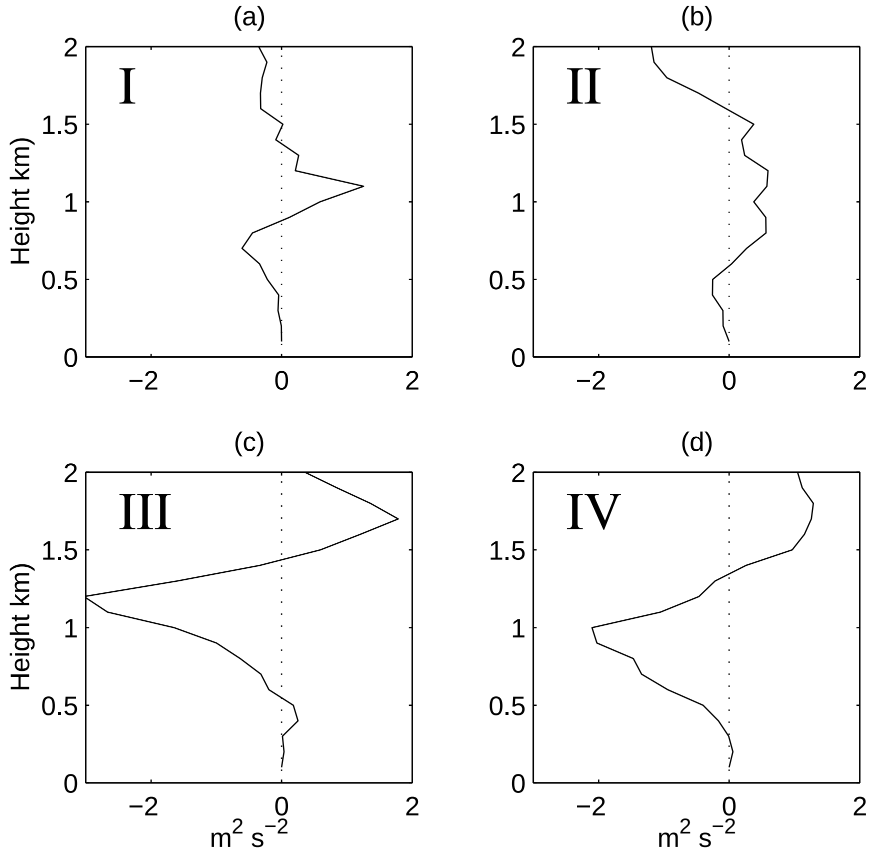

Figure 3.9: Momentum flux profiles averaged over the individual billows shown in Fig. 3.8.

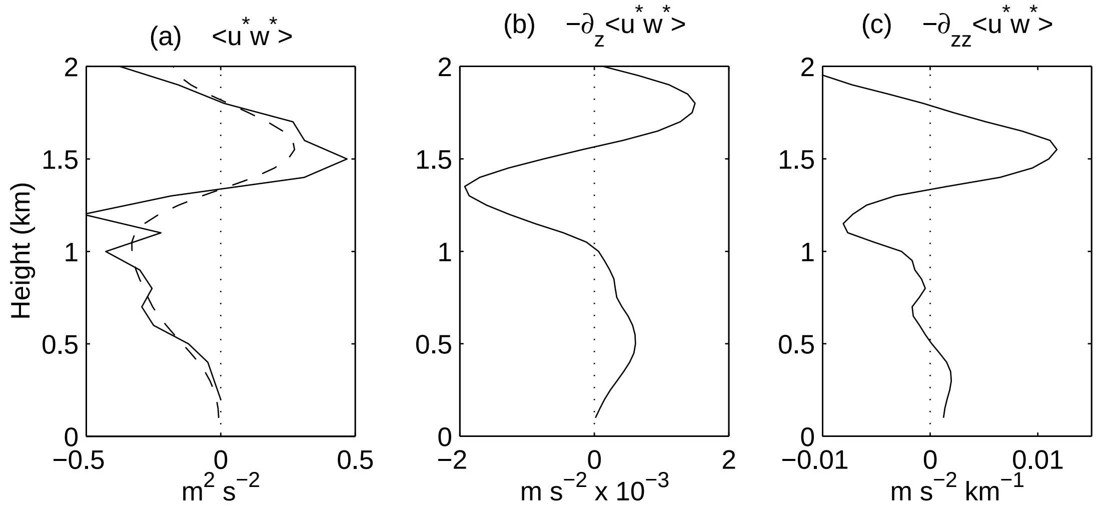

Figure 3.10: (a): Momentum flux profiles averaged over six billows (see text) east of radar between 2200 and 2220 UTC (solid line). Dashed line is a smoothed fit to the actual data. (b): Momentum flux convergence, derived from (a). (c): Vertical derivative of the momentum flux convergence, derived from (b).

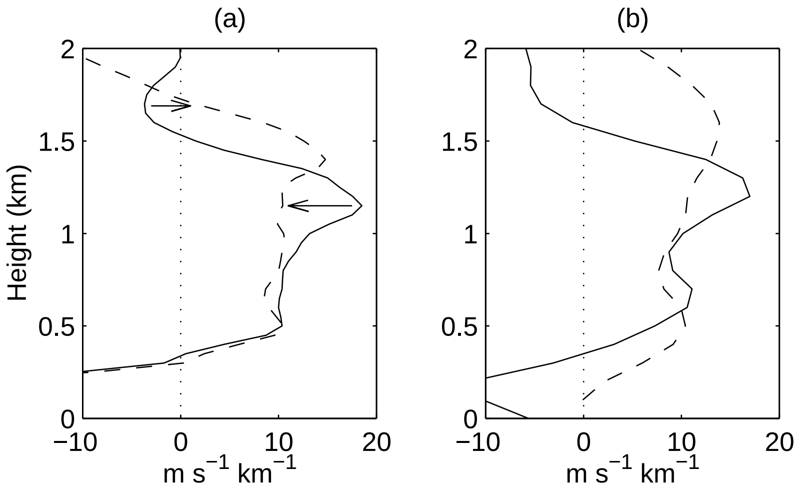

Figure 3.11: (a): Wind shear profiles at locations 5 km south and 5 km north (solid and dashed curves, respectively) of the initial shear profile, obtained by integrating the profile in Fig. 3.10(c). (b): Wind shear profiles measured within (solid lines) and downwind (dashed lines) of billows, reproduced from Figs. 3.6(a) and (b) for comparison with (a).

Figure 3.12: PPI of reflectivity at 2145 UTC at an elevation of 0.5°.

Figure 3.13: Plan view of the locations of the reflectivity cores and bands at around 2210 UTC, subjectively determined from RHIs such as those shown in Fig. 3.14. Circles mark the eastern edge of the reflectivity cores. Solid lines indicate the bands. Dotted lines indicate the position of the RHIs used. No reflectivity cores could be identified in RHIs further north than shown here.

Missing Figure

Figure 3.14: RHIs of reflectivity at an azimuth of 90° at (a) 2200, (b) 2210 and (c) 2220. Superimposed are contours of vertical velocity where it is greater that 1 m s^{-1}. The contour interval is 0.5 m s^{-1}. The vertical velocity has been calculated assuming it is zero at 0.2 and 3 km, as described on page 50.

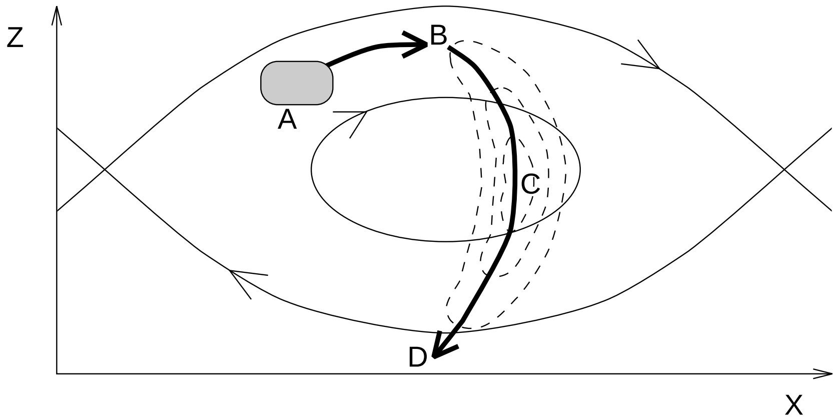

Figure 3.15: Schematic diagram showing the stages in the production of the reflectivity echos (dashed lines) which based on those shown in Fig.3.14. The bold lines indicate trajectories of the droplets responsible for the reflectivity core. Further details are given in the text.

CHAPTER 4

Potential Shearing Instability

4.1 Introduction

This chapter continues to look at the case studied in the previous chapter, but focusses on the larger scale processes that caused the billows to occur where they did. Roach (1970), Bosart and Garcia (1974) and Keller (1989) have attempted, with mixed success, to relate areas containing billows and CAT to indices diagnosed from larger-scale properties of the flow in the upper troposphere. Billows may also occur due to vertically propagating gravity waves breaking at their critical level (e.g. Fritts *et al.* 1996b), possibly in a location related to the orography. Here it is suggested that, in addition to these locations, billows may be a fairly common (but hitherto largely unobserved) feature of surface warm fronts.

It will be shown that the role of moisture at the front is important, both in causing billows to occur, and in enabling them to have a large depth (comparable with the depth of the frontal zone itself). Thus large-amplitude billows may cause considerable vertical mixing within a significant proportion of warm fronts, and this mixing may itself substantially alter the structure of the frontal zone. This case study demonstrates the existence of a latent shearing instability, which is released when a layer is lifted to saturation. We refer to this as potential shearing instability (PSHI).

A schematic diagram showing the location and orientation of billows relative to the front with which they were associated is shown in Fig. 4.1 (quantitative aspects are discussed later). The locations of billow "crests" were determined as described in the previous chapter. As mentioned previously, the surface front, defined by sharp gradients in the wind field from radar observations, moved northwards at around 10 m s^{-1}. Fig. 4.1 indicates that the radar was capable of resolving the billows well only at close range, as they passed close to the radar site. It seems likely that

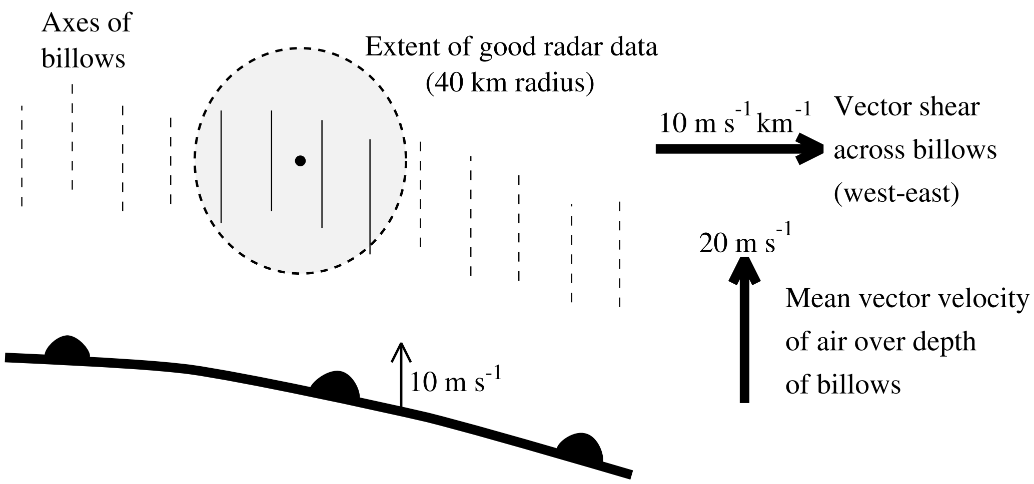

Figure 4.1: Schematic diagram showing the extent of radar coverage, the observed location of billow axes (shown by solid lines) and the likely location of the billows (dashed lines) in relation to the surface warm front.

billows existed along other parts of the front (in a strip moving with the surface front, continuing beyond the range of the radar) and also at earlier times, when this strip was beyond the range of the radar. Owing to the nature of the air flow within the billows, they are most evident in the Doppler data when observations are made perpendicular to their axes. There is no Doppler evidence of them when observations are made along their length.

As described in Chapter 3, west-east scans were made by the radar as the train of billows advanced northwards, towards and then over the radar site. Plan views showing the billows crests were constructed for all the scanning sequences in Table 3.1. These showed that there was considerable variation in the along-axis length of the billows, ranging from around 10 to 40 km. An accurate measurement of the mean length could not be made, as many of the billows lay partly outside the region scanned by the radar, but a subjective estimation of around 30 km is reasonable. The train of billows as a whole had a south-north extent slightly greater, around 40 km, due to variation in the location of individual billows. The overall train of billows existed for all the time that the radar was capable of observing them (3 hours). This is considerably longer than the residence time of air parcels within individual billows which, since the air was moving along their axes at a relative speed of 10 m s^{-1}, was around 50 minutes. Browning and Watkins (1970) observed billows of a similar amplitude complete their lifecycle over a period of 10 minutes. Evidently the larger-scale flow was acting to sustain the shearing instability over a longer period in the present study.

The rather piecemeal nature of the radar observations of the billows and the environment, together with the lack of sufficiently detailed thermodynamic measurements from radiosonde ascents distant from the radar, makes it impossible to determine precisely the environment in which the billows occurred using observations alone. The mesoscale version of the U. K. Meteorological Office Unified Model (UM) has been used to fill in these gaps in the observations, allowing the relevant process to be determined.

4.2 The role of the mesoscale structure in determining the location of billows

4.2.1 The mesoscale model

The version of UM used here is essentially as described by Cullen (1993). To summarise, the mesoscale version of the model, which is nested inside the limited-area model, uses a hybrid vertical coordinate which is terrain-following in the lower layers of the atmosphere. It has 31 levels in the vertical, with a resolution of around 60 m at the surface, and 350 m at an altitude of 2 km (Figure 4.2). A regular latitude-longitude grid is used in the horizontal, with a resolution of 0.15° (corresponding to approximately 16.8 km). It takes its lateral boundary conditions from a coarser-resolution limited-area model in which it is nested. In the boundary layer, vertical turbulent transport of quantities is implemented by a diffusion dependent on the height, surface roughness, and local static stability and shear (and thus the local Richardson number). These transports are calculated taking into account the presence or absence of cloud and thus the effect of latent heat release on the static stability. Outside of the boundary layer, i.e. in the free troposphere where the process described in this chapter occurred, there is no such calculation, and no artificial vertical diffusion is explicitly imposed (other than that resulting from the numerical schemes used in the model). Horizontal smoothing is carried out on all fields for computational reasons, using a fourth order diffusion scheme.

p (mb)	z (m)	Δz (m)	p (mb)	z (m)	Δz (m)
997	24	60	822	1544	248
989	83	74	795	1812	299
978	172	101	762	2142	364
964	286	123	725	2541	438
948	418	142	682	3018	524
930	569	159	635	3589	626
911	736	174	582	4271	733
890	916	186	527	5055	827
869	1109	200	472	5925	949
846	1317	217	415	6952	1027

Missing Figure

Figure 4.2: Table and graph showing the approximate heights and spacings of the lowest 20 levels in the mesoscale version of the Unified Model, assuming a surface pressure of 1000 mb.

The data used in this study come from the 1800 UTC operational run of the model on 6 September 1995. As comparisons between the model and observations are made at 2200 UTC, this allows the model 4 hours to "spin up" to give a realistic representation of the atmosphere.

4.2.2 The warm frontal structure as determined by the mesoscale model

Fig. 4.3 shows a plan view of the rain rate derived from the FRONTIERS network, the mesoscale model's mean sea-level pressure and the analysed position (from the model) of the surface warm front (SWF) at 2200 UTC. This figure also shows the location of south-north cross-sections of model data centered on Chilbolton radar which are given in Fig. 4.4(a)-(d). These show details of wet bulb potential temperature (θ_w), relative humidity (RH), west-east component of the wind (u), and front-relative wind arrows projected onto this section. They indicate the following features of the front:

- Warm, moist air approached the SWF at low levels (below 1 km) from the south, and then rode up over the frontal zone, retaining an eastward component as it did so.

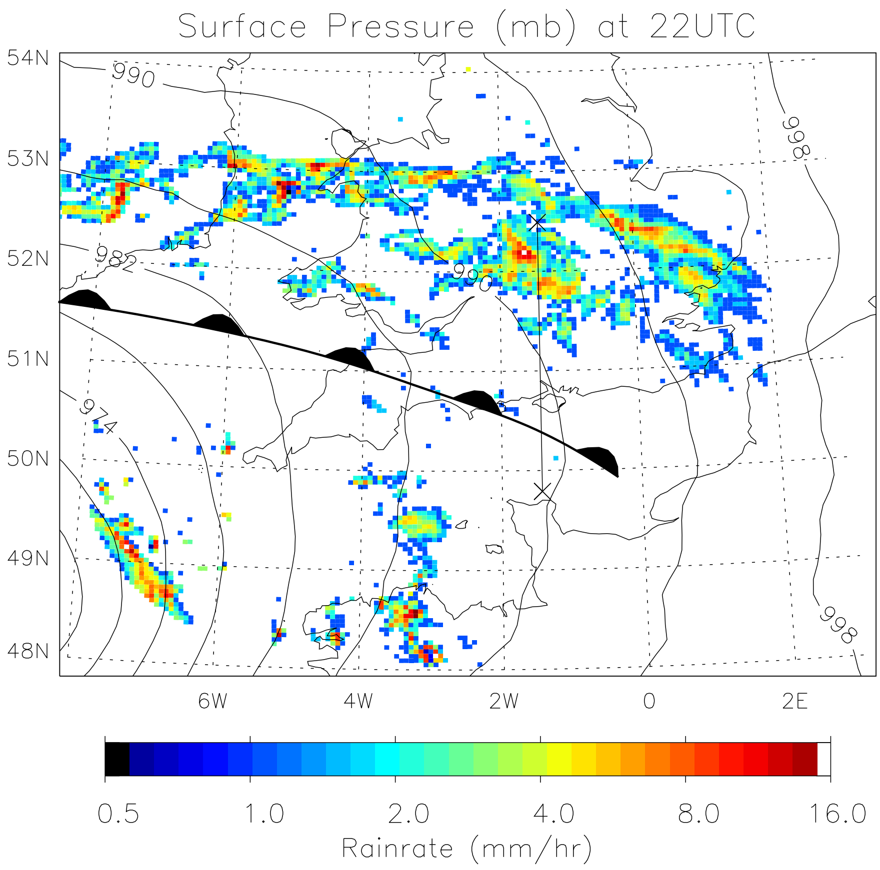

Figure 4.3: Mean sea-level pressure and the analysed position of the surface warm front from a 4-hour forecast by the mesoscale model, valid at 2200 UTC, 6 Sept. 1995. XX shows the position of the cross-sections in Fig. 4.4. The rain rate from the FRONTIERS network at the same time is shown shaded.

- Cold, and initially dry air ahead of the surface warm frontal zone travelled westwards, approaching it at low levels. As it entered the lower part of the frontal zone, it rose and then moved northwards retaining its westward component as it did so.

- Air within the frontal zone itself originated mainly from the boundary layer just ahead of the SWF.

- The warm and cold air had a relative motion that was broadly consistent with the thermal wind relation, so the change from an easterly to westerly component with height just north of the SWF was related to the temperature gradient across the front.

An upper cold front (UCF) existed ahead of the SWF, with banding in the cloud and precipitation similar to that described by Browning *et al.* (1973). Behind the UCF the dry low-θ_w air

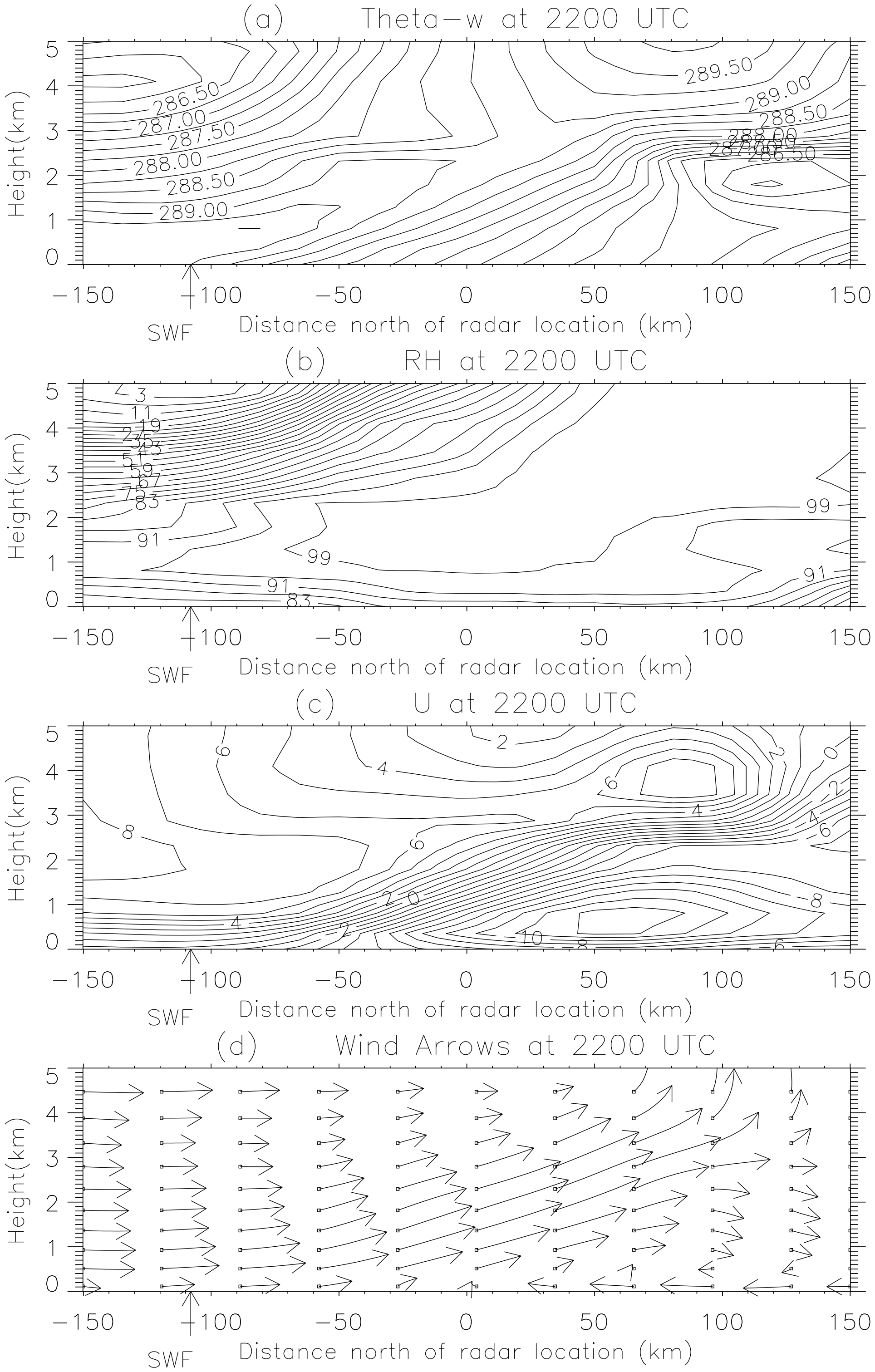

Figure 4.4: Vertical cross-sections from the mesoscale model at 2200 UTC, 6 Sept. 1995 along the line XX in Fig. 4.3 which passes through Chilbolton radar. (a): Wet-bulb potential temperature, θ_w (K). (b): Relative humidity with respect to ice (%). (c): West-east component of the wind, u (m s^{-1}, +ve out of the plane). (d): Front-relative wind arrows, the length of each indicating parcel displacements over a period of 1 hour.

overriding the moist warm-sector air gave rise to potential instability, where $\partial\theta_w/\partial z$ is negative. The convective cells referred to earlier (and described in detail in Chapter 3) were due to the release of this potential instability.

4.2.3 Validation of the larger-scale thermodynamic features reproduced by the model

Figure 4.5 shows time-height plots of θ_w, from (a) the mesoscale model and (b) radiosonde data from Herstmonceaux, both at 0.3°E, 50.9°N, 120 km to the east of the radar and the cross-sections in Fig. 4.4. Warm air is shown shaded in the section from the model. The two sections show good agreement in the following respects:

- The SWF passes over Herstmonceaux at the same time (0200 UTC $\pm$ 1 h).
- θ_w at the SWF is within 0.5 K of 288.5 K.
- The ascent at 2000 UTC gives a similar depth between 287 and 289 K through the front, although the layer between these two temperatures in the model is slightly higher and deeper.

Thus the model is interpreted as having reproduced actual thermodynamic structures well, locating them to within around $\pm$ 90 minutes. Using the observed speed of the surface front, this corresponds to a distance of approximately 55 km, which is 3 model grid lengths. Unfortunately no data were available with good temporal coverage from stations closer to the radar than Herstmonceaux, which is why this study is so reliant on the mesoscale model data.

4.2.4 The model's detailed representation of the frontal zone and the adjustments required to fit the observations

Section 4.2.3 has demonstrated that the model and the observations were broadly consistent. However, in order to relate the radar observations of the billows to the model we need to obtain consistency on scales of order 10 km. The aim of this section is to show how the model, which

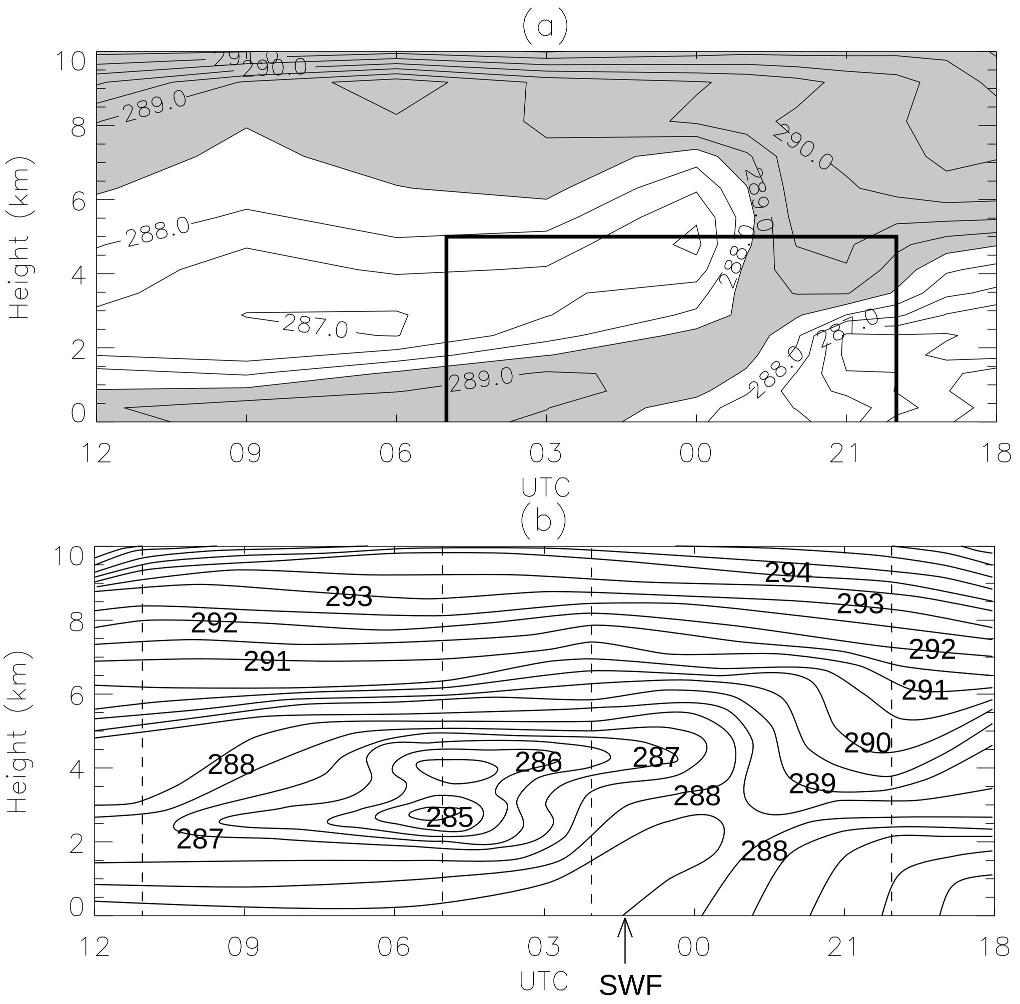

Figure 4.5: Time-height sections of θ_w above Herstmonceaux on 6/7 Sept. 1995, derived from (a) mesoscale model and (b) radiosonde ascents. The warm air ($\theta_w > 288.5$K) is shown shaded in (a). The times of radiosonde ascents are indicated by the dashed lines in (b). Owing to the sparcity of data in some regions of (b) the mesoscale model has been used to help interpolate the radiosonde data in a realistic way (although the contours still fit the radiosonde data at the times of ascents). The equivalent location of distance-height cross-sections in Figs. 4.4, 4.6 and 4.8 are shown by the rectangle in (a).

yields both thermodynamic and kinematic fields, has been adjusted slightly so that it is consistent on these scales with the kinematic fields obtained from the radar, and other observations. This adjustment has been done to obtain the "best estimate" of the state of the atmosphere at the exact time and place where the billows are known to have existed.

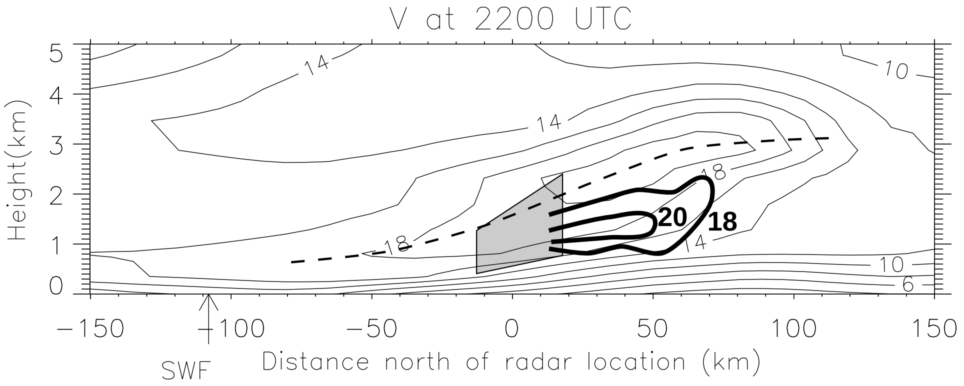

Figure 4.6: South-north cross-section at 2200 UTC, 6 Sept. 1995, along the line XX in Fig. 4.3 showing the southerly component of wind, v (m s^{-1}) from the mesoscale model (thin lines). The model's jet axis is shown dashed. Superimposed are two contours (18 and 20 m s^{-1}) of the same component of the wind measured by the radar (bold lines). The location of the billows is shown shaded.

Comparisons between model fields and observations

(i) *Comparison of the model's southerly wind component (v) with that measured by the radar.* Figure 4.6 shows a cross-section of the southerly (front-normal) component of wind from the model and radar at 2200 UTC. The main feature is the low-level "jet" of warm air which rides up over the frontal zone. In the model and radar data, this jet has a similar shape, slope and magnitude, with a maximum of around 20 m s^{-1}. However, the location of the jet axis is displaced in the model relative to the radar. This displacement could be due to the model having located the frontal system (1) too far south by approximately 40 km, or (2) too high by approximately 800 m, or a combination of (1) and (2). Evidence given below in Section 3(d)(2) suggests that (1) is more likely.

(ii) *Comparison of the model's westerly component of the wind shear ($\partial u/\partial z$) with that measured by the radar.* We compare in Fig. 4.7 the wind shear profile ($\partial u/\partial z$) derived from radar data within the billows with the two corresponding model wind shear profiles derived assuming (1) and (2) above respectively. The radar observations (Fig. 4.7(c)) show a maximum in the vertical wind shear at a height of 1.2 km. The corresponding maximum occurs at heights of 0.8 km and 0.5 km in Figs. 4.7(a) and (b) respectively. The closer fit of (a) supports assumption (1), implying that the model mislocated the front by around 40 km to the south. This is consistent with the

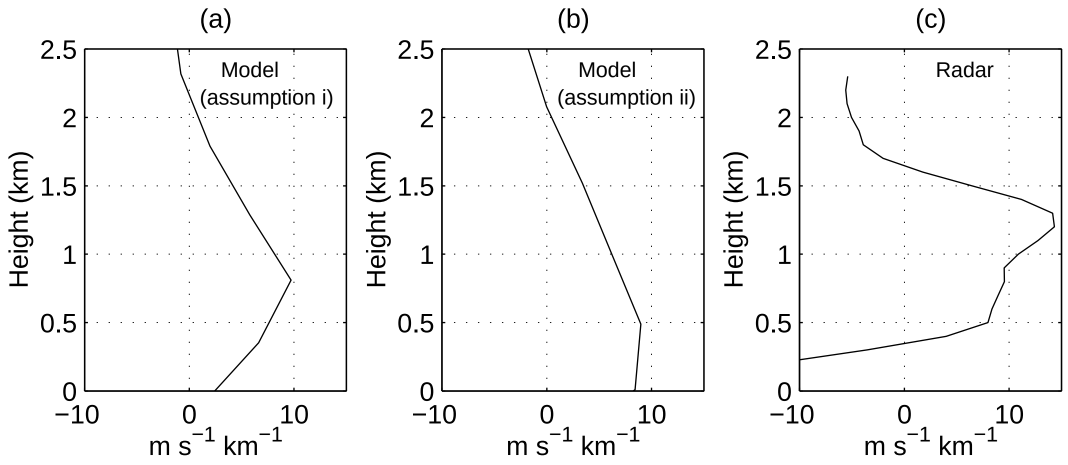

Figure 4.7: Vertical profiles of the westerly component of the vertical wind shear ($\partial u/\partial z$) at 2200 UTC, 6 Sept. 1995, in the region of the billows. (a) and (b): Model-derived profiles obtained after adjusting the model according to assumptions (i) and (ii), respectively (see text). (c): Radar-derived profile based on radar data averaged over times 2200, 2210 and 2220 UTC, and averaged over 12 km close to the radar.

resolution of the model, as a displacement of 40 km horizontally implies an error of only 2 grid lengths. However, there are 4 model levels between 1.0 and 1.8 km, so a vertical displacement seems less appropriate in any case.

In addition, the shear layer responsible for the billows was spread out over a greater depth in the model, possibly as a result of excessive *horizontal* diffusion which then affected the shear layer depth via the slope of the frontal zone. As a consequence, the peak shear was only around 10 m s^{-1} km^{-1} in the model (Fig. 4.7(a)) compared to 14 m s^{-1} km^{-1} in the profile derived from the radar data (Fig. 4.7(c)).

(iii) *Comparison of the model's relative humidity with observations from synoptic reporting stations.* As we shall see later, the behaviour of the billows depended critically on the level of saturation (i.e., the cloud base) and so it is important to adjust any small errors that there may have been in the model's relative humidity field, especially at low levels where the billows occurred. The model cross-section showing RH in Fig. 4.4(c) indicates a cloud base, assuming that this is given by the 99% contour, at around 900m. However, synoptic observations at this time indicate that the cloud base north of the SWF was lower than this, at approximately 400m.

Adjustment of the model fields.

Section 4.2.3 has validated the model on scales greater than 100 km horizontally, and 500 m vertically. The comparisons made in Sections 4.2.4 and 4.2.4 indicate the need for all of the following finer scale adjustments:

- displace all model fields 40 km north to agree with Doppler radar observations of the kinematic structure of the front;
- increase model shear by a factor of 1.4 in the frontal zone, to agree with radar observations of the shear responsible for the billows;
- reduce height of $RH = 99\%$ contour by 400 m to around 400 m, to agree with cloud base observations.

By adjusting the model output in this way, the resulting fields will be more accurate (though less balanced) than the raw model fields, and of course much more comprehensive than the actual observations. The discrepancy that is introduced in the location of the northern end of the south-north jet may be explained as the result of the mixing by the billows not being represented by the model.

Figure 4.8(a) shows the resulting adjusted model fields of θ_w and $RH = 99\%$ in the region of the surface warm front, including the location of the observed billows and the front-relative airflow into them. The causal relationship between these fields and the location of the billows will be discussed later in this chapter.

4.2.5 Calculation of the Richardson number

The Richardson number is defined as the ratio of the static stability to the vertical wind shear. However, in this case the evaluation of Ri appropriate to the billow formation is complicated by two factors: (i) the proximity of the frontal shear zone to the strong differently orientated shear in the boundary layer, and (ii) the saturation of much of the frontal zone.

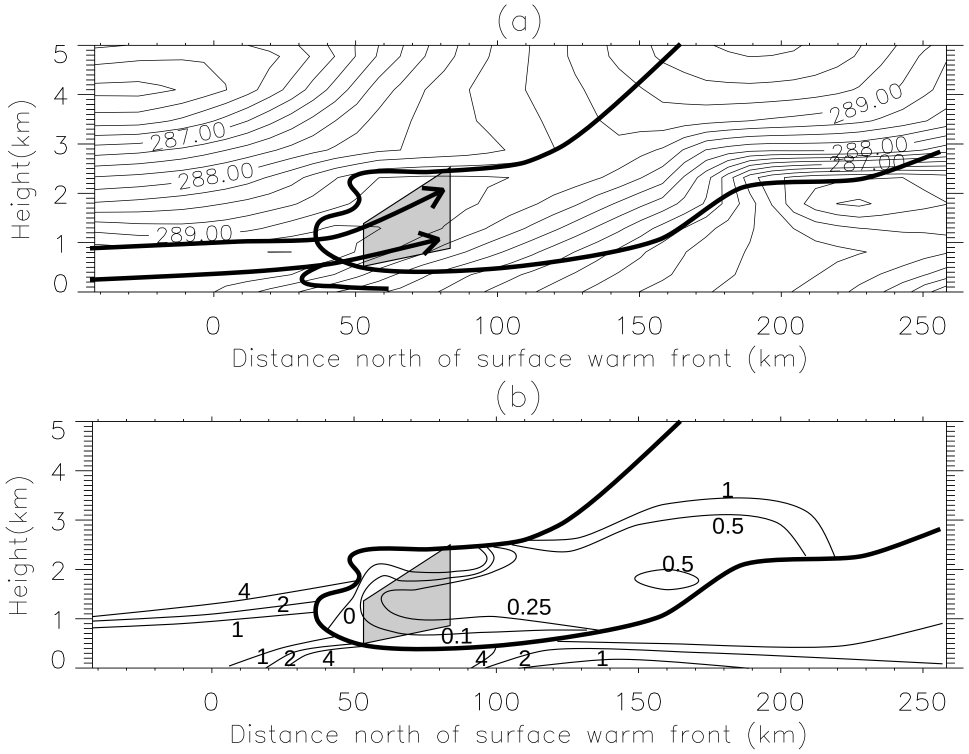

Figure 4.8: South-north vertical cross-sections (passing through Chilbolton radar) at 2200 UTC, 6 Sept. 1995, showing fields adjusted as described in the text. The fields shown are (a) wet-bulb potential temperature and front relative streamlines entering the region containing the billows and (b) Richardson number Ri_x as defined in the text. The effective region of saturation (RH>99%) is delineated by a bold contour, and the location of the billows is shows shaded, in both (a) and (b).

The problem of the variable orientation of the shear vector.

The hodograph shown in Fig.3.3 indicates that there was a strong south-north component of wind shear between the ground and a height of 0.6 km, which would have been associated with relatively small-scale turbulent mixing in the boundary layer. The strong west-east component of shear responsible for the observed large-amplitude billows existed between 0.4 and 1.6 km. Although the lower portion of the billow shear layer, between 0.4 and 0.6 km, slightly overlapped with the boundary-layer induced shear, most of the billow layer, between 0.6 and 1.6 km, was characterized by an almost zero component of shear in the south-north direction. The south-north component of the wind shear has been neglected in the following calculations of *Ri* since it is only the instability of the flow to large-amplitude billows that we are concerned with in this study. By calculating Ri_x rather than Ri we greatly increase the apparent Richardson number in the boundary layer, but the value in the frontal zone is close to the actual Richardson number because of the very small south-north component of shear over the layer containing billows. All references to the Richardson number in the following refer to Ri_x.

The effect of saturation on the static stability.

The static stability has been defined as

$$N^2 = N_d^2 = \frac{g}{T}\left(\frac{dT}{dz} - \Gamma_d\right) = \frac{g}{\theta}\frac{d\theta}{dz} \tag{4.1}$$

where the air is unsaturated (RH <99%). However, for a given temperature profile, the atmosphere will always have a reduced static stability if it is made saturated, due respectively to the release and absorption of latent heat accompanying upward and downward air-parcel displacements. Although for large vertical displacements the evaporation of water droplets may be too slow to maintain saturation, it is reasonable to assume that, in the early stages of the growth of an instability, small downward displacements by an air parcel can maintain saturation by rapid evaporation of the smallest cloud droplets. In regions where the air is saturated (RH >99%) the static stability has been defined as (Lalas and Einaudi 1974)

$$N^2 = N_w^2 = \frac{g}{T}\left(\frac{dT}{dz} - \Gamma_w\right)\left(1 + \frac{Lq_s}{RT}\right) - \frac{g}{1+q_w}\frac{dq_w}{dz} \tag{4.2}$$

where q_s is the saturation mixing ratio, and q_w is the total water mixing ratio. The multiplying factor in the second bracket comes from the virtual temperature effects of the water affecting the equation of state. The final term takes into account the vertical gradient of the background mixing ratio. All the relevant terms are available in the UM output. This expression for N_w^2 was shown by Durran and Klemp (1982) to be the correct value, and much better than an approximation obtained by a simple substitution of θ_w for θ in (4.1).

Ri_x was calculated at 50 mb intervals, using a centered difference approximation over depths of 100 mb (corresponding to a height interval of around 800 m), which is comparable to the observed depth of the billows. The result is shown in Fig. 4.8(b). The different definitions of N^2 in the saturated and unsaturated regions lead to the discontinuities at the cloud boundary.

4.2.6 The aspects of the mesoscale frontal structure that determined the location of billows

Figure 4.8 shows the best estimate of the relevant thermodynamic and kinematic fields in the frontal zone at the time of the billows. The processes leading to the development of the billows can be inferred from these fields.

High-θ_w air which approached the frontal zone from behind (i.e. south of) the surface front (upper bold arrow in Fig. 4.8(a)) was initially unsaturated. Ascent occurred in association with convergence near the surface front, and above 500 m the air became saturated as it flowed northwards. Lower-θ_w air which approached the frontal zone at low levels (in the boundary layer) from the north was also unsaturated. Close to the surface front, this air mixed with warmer air and then it too ascended (lower bold arrow in Fig. 4.8(a)), becoming saturated as it travelled upward and northward conserving its θ_w.

These two air-streams, represented by the two bold arrows in Fig. 4.8(a), were in relative motion in the direction perpendicular to the cross-section, broadly in agreement with the thermal wind relation. This gave rise to the strong shear layer between them. This is the shear layer that caused the large-amplitude billows to occur. If the air had been dry, then the sheared layer would have had a minimum Richardson number of around 1 over a depth of 800 m. However, the air was saturated, and so the layer had a Richardson number of between 0 and 0.25 when measured over 800 m increments (Fig. 4.8(b)), consistent with the observed occurrence of large-amplitude billows.

The location of initiation of billows in the frontal region, according to the analysis, was dictated by the height of the $RH = 99\%$ contour (although the height of this contour itself may in turn have been affected to some extent by the presence of the billows). Upstream of the billows, while the flow was still unsaturated, the shear was allowed to become large whilst the dry Richardson number remained well above 0.25. The Richardson number when calculated assuming the air was moist in this location was, however, less than 0.25. This potential for instability was then released "immediately" the air became saturated, initiating billows over a considerable vertical depth of 1 km, with an initial minimum Richardson number well below 0.25.

4.3 Discussion

The large-amplitude billows were observed in a location just north of a surface warm front, which coincided with the onset of saturation due to ascent at the surface front. The onset of saturation suddenly lowered the Richardson number of a deep sheared layer in the frontal zone from around 1 to a value much less than 0.25. This statement is supported by the estimation of the lifetime of the billows, made in Chapter 3. A lifetime of 50 minutes is very long compared to other observations such as those made by Browning and Watkins (1970), who found the lifetime of their otherwise similar billows to be 10 minutes. However, Thorpe (1973a) found that the time taken for the billows to collapse back to parallel flow was inversely proportional to the Richardson number, so a long lifetime implies that the initial Richardson number was substantially less than 0.25. Scinocca (1995) also found the same relationship between lifetime and Richardson number in his numerical modelling study.

The presence of saturation in the frontal zone was critical not only to the location but also to the intensity, vertical extent and duration of the billows that developed. In the absence of the sudden development of instability over a deep layer due to the onset of saturation, and in the absence of a rapid dynamically-induced increase in shear, it is likely that a critical Richardson number and associated billows would appear first over a shallower layer or layers.

The dependence of the dynamic stability of a stratified shear layer on its saturation is analogous to conditional instability (CI), which describes the dependence of the static stability of a parcel on its saturation. A temperature profile exhibits CI at a particular height if the air is statically stable at that height when the air is unsaturated, and statically unstable when the air is saturated, i.e.

$$\Gamma_{sat} < \Gamma < \Gamma_{dry}$$

where Γ_{sat}, Γ and Γ_{dry} represent the saturated, environmental and dry lapse rates ($-\partial T/\partial z$), respectively. Likewise, a combined temperature and velocity profile exhibits what we may define as conditional shearing instability (CSHI) at a particular height if the air is dynamically stable at that height when the air is unsaturated, and dynamically unstable when the air is saturated, i.e.

$$Ri_{sat} < Ri_{crit} < Ri_{dry}$$

where Ri_{dry} and Ri_{sat} represent the gradient Richardson number calculated assuming the air is dry and saturated using values of static stability calculated from (4.1) and (4.2), respectively. Ri_{crit} represents the critical Richardson number, which will in general be a little less than 0.25.

Similarly there is an analogy between potential instability (PI) and what we define as potential shearing instability (PSHI). PI exists over a layer in the atmosphere when the layer would be statically unstable if it were lifted to saturation. This might occur if the lower part of the layer became saturated before the upper part. The condition for PI to exist is $\partial\theta_w/\partial z < 0$. PSHI exists over a layer if the layer would become dynamically unstable, but not statically unstable, when it is lifted to saturation (assuming the shear over the layer remains constant). The layer does not need to exhibit CSHI at its original height for this to occur (although it may do) as the lower part of the layer may become saturated before the upper part due to a vertical gradient in relative humidity. This could dynamically destabilise the layer, without making it statically unstable.

In the case described, flow into the region containing billows was along the contours of the front-parallel component of wind (Fig. 4.4), indicating that the shear over the layer which became responsible for the billows was conserved as the layer was lifted to saturation. This layer therefore exhibited PSHI upstream of the billows, as well as CSHI. The concept of PSHI allows us to see that a dynamically stable layer can exhibit a latent dynamical instability. Only through lifting to saturation can this instability be released. This could, for example, also occur in a layer forced to ascend over or downwind of orography, making billows visible on the edges of orographic clouds

Missing Figure

Figure 4.9: Contours of the Richardson number (solid and dashed lines indicating positive and negative values, respectively) calculated over the layer described in the caption to Table 4.1 after it has been lifted to saturation. Dotted contours give Δp_{sat}, the pressure change (in mb) over which saturation occurs (negative values indicate that the top of the layer reaches saturation before the bottom). The Richardson number calculated over the original, dry, layer is shown at the bottom of the figure for each value of T_{top} (being independent of q_{bot})

(e.g. Reiter *et al.* 1969).

Unfortunately it is not possible to derive a simple criterion for PSHI which is analogous to the θ_w criterion given above for potential instability because of the need to integrate along saturated adiabats. However, if it is assumed that the wind change over the depth of a layer does not change when the layer is lifted, then the stability of a layer of air may be derived using a tephigram, or an algorithm which can be implemented on a computer. The latter has been used to produce Fig. 4.9 and Table 4.1.

For the particular layer looked at (details given in the table caption), T_{bot} and q_{top}, T_{top} and q_{bot} must lie within a fairly narrow range in order that PSHI occurs (indicated by the three Richardson numbers in bold type). The conditions for PSHI clearly lie in between the conditions necessary for a layer to be unstable and moderately stable to potential instability, and since both these situations occur frequently in the troposphere, the conditions necessary for PSHI will not be unrealistic. This is shown in Fig. 4.9, where T_{top} and q_{bot} must lie within the bold contours for PSHI to occur. The bounds on T_{top} and q_{bot} for PSHI to occur become much less restrictive as the shear across the layer is increased without changing any of the other properties of the layer.

Of the three cases of PSHI shown in the table the one with $T_{top} = 7°\text{C}$ and $q_{bot} = 6\text{g kg}^{-1}$ is the one that is most likely to produce intense large-amplitude billows. Initially it is stable, with a

		Original		If saturated		After lifting to sat.			
q_{bot}	T_{top}	N^2	Ri	N^2	Ri	N^2	Ri	p_{sat}	Δp_{sat}
5	5	1.40	1.06	-0.11	*-0.08*	0.21	**0.18**	910	-13
5	6	1.79	1.36	0.34	0.26	0.45	0.39	910	1
5	7	2.19	1.67	0.81	0.62	0.69	0.61	899	11
5	8	2.59	1.97	1.28	0.97	0.92	0.83	887	23
5	9	2.98	2.27	1.75	1.33	1.11	1.06	875	35
6	5	1.40	1.06	-0.11	*-0.08*	-0.38	*-0.32*	924	23
6	6	1.79	1.36	0.34	0.26	-0.14	*-0.12*	911	36
6	7	2.19	1.67	0.81	0.62	0.10	**0.09**	899	48
6	8	2.59	1.97	1.28	0.97	0.33	0.30	887	60
6	9	2.98	2.27	1.75	1.33	0.56	0.52	875	72
7	5	1.40	1.06	-0.11	*-0.08*	-0.95	*-0.80*	924	57
7	6	1.79	1.36	0.34	0.26	-0.71	*-0.61*	911	69
7	7	2.19	1.67	0.81	0.62	-0.47	*-0.42*	899	81
7	8	2.59	1.97	1.28	0.97	-0.24	*-0.22*	887	93
7	9	2.98	2.27	1.75	1.33	-0.01	*-0.01*	875	105
7	10	3.38	2.57	2.24	1.70	0.22	**0.21**	864	117

Table 4.1: Static stability and Richardson numbers for a layer of air 100 mb deep, over which there is a velocity change of 10 m s^{-1}. Richardson numbers are in bold if they lie between 0 and 0.25, and italics if negative. Originally the layer is between 1000 and 900 mb, the temperature at the bottom of the layer is 10°C and the mixing ratio at the top of the layer is 4 g kg^{-1}. The first two columns give the mixing ratio at the bottom and the temperature at the top of the layer in these units. The next two columns give the static stability (in 10^{-4}s^{-1}) and Richardson number calculated over the layer which is unsaturated. The next two columns give these parameters calculated assuming the layer *is* saturated. The next two columns give these parameters after the original layer has been lifted to a level at which it just becomes saturated over its whole depth. The final two columns give the pressure (in mb) of the base of the layer at this stage, and Δp_{sat}, the pressure change (in mb) over which saturation occurs (negative values indicate that the top of the layer reaches saturation before the bottom).

Richardson number considerably greater than 0.25. It does not exhibit CSHI, as if it were made saturated without lifting then it would still have a super-critical Richardson number. If it were to be lifted by 51 mb, the base of the layer would just become saturated. The remainder of the layer would then become saturated after a further 48 mb (last column in table), allowing the layer to develop a very low sub-critical Richardson number over a fairly short period of time, given sufficient lifting of the layer by the environmental flow.

If the layer is initially more stable ($T_{top} = 10°$C and $q_{bot} = 7$g kg^{-1}) then saturation of the bottom of the layer must occur earlier in the lifting process in order that the stability of the layer may be reduced sufficiently. As a result, the saturation of the layer occurs over a much greater depth, and thus on a time-scale which may not allow a very low Richardson to develop. Again, this layer does not exhibit CSHI at its original level.

The layer with $T_{top} = 5°$C and $q_{bot} = 5$g kg^{-1} exhibits PSHI which is released over a depth of only 13 mb. This layer is in fact conditionally unstable at its original level, and is *stabilised* by lifting to saturation, as the top of the layer becomes saturated before the bottom. The decrease in Richardson number is thus due only to the saturation of the layer as a whole, rather than differential saturation of the layer during lifting.

Unfortunately, the flow through the warm front studied here is not simple enough for the above calculation to be made upstream of the billows. This is because the flow into the region containing billows came from both ahead and behind the surface front, and saturation occurred at a low level. If the air entering the frontal zone had had a lower moisture content, then saturation would have occurred higher and further north of the front. In such a situation, the calculations described above would have been more relevant. However, the idea of PSHI is still valid even in this case, as it refers to the physical process which was occurring.

The warm front described, although a strong one associated with an ex-tropical cyclone, is not extraordinary, either in terms of the wind shear across it, or of the thermodynamic structure. It therefore seems likely that PSHI would exist and be released in many other warm fronts where ascent at the surface front induces saturation. Although billows are difficult to observe, there are a small number of published observations which appear to support this hypothesis. For exam-

Missing Figure

Figure 4.10: (a) Doppler velocity and (b) vertical shear through billows observed at 1610 UTC on 11 February 1997. The patterns in these two RHIs are not as clear as in the September case partly because scans could not be made exactly perpendicular to the billow axes. The speckled region is due to noise where no data were available as a result of insufficient precipitation.

ple, Browning *et al.* (1970a) made Doppler radar observations in two precipitating warm frontal zones. Fairly large amplitude billows (with wavelengths up to 5 km) were observed ahead of the surface warm front, and can be seen in a cross-section parallel to the surface front in Fig. 7 of their paper. The billows observed by Bryant and Browning (1975) using Doppler radar occurred in a precipitating warm frontal zone, just ahead of the surface front. The layer containing billows had been brought to saturation at the time when they were observed. They were orientated perpendicular to the surface front, and, again, were caused by the component of shear parallel to the front. Wakimoto *et al.* (1992) observed large amplitude billows within a few kilometers of an extremely sharp warm front. Near to the surface, the frontal slope was steeper than 1:10, so saturation presumably occurred suddenly as air entered and ascended through the frontal zone. This conclusion is supported by the existence of a well-defined line of convection along the surface warm front. Takahashi *et al.* (1993) observed large-amplitude billows within a precipitating shear layer orientated parallel to a stationary surface front. Although not directly related to PSHI, Wang *et al.* (1983) observed long wavelength (12-19 km) billows within a precipitating warm frontal zone. They suggested that these waves may have been one of the resonant modes referred to in the Introduction, and noted that the Richardson number calculated over the layer containing billows was sub-critical only if the effect of moisture was included.

In addition to these previously published observations and the main case study presented here, Figs. 4.10(a) and (b) show RHIs of Doppler velocity and vertical shear obtained in another warm frontal case on 11 February 1997, during FASTEX. The billows apparent in these RHIs again occurred in a precipitating warm frontal zone just ahead of the surface warm front. The mesoscale model's representation of this front (not shown) revealed that the air entering the region containing billows had been lifted to saturation by ascent at the warm front, although in this case the level of saturation was very close to the ground.

Studies of turbulent dissipation of kinetic energy in the free troposphere have tended to concentrate on the dissipation by CAT, which is most likely to occur at upper level frontal zones and near the tropopause close to jets. The stronger winds at upper levels than at lower levels might at first appear to suggest that the energy dissipation in the free troposphere would be dominated by the contribution from higher levels. However, strong shears also occur in low-level frontal zones and the onset of saturation near surface fronts allows PSHI to be released over large depths, so significant mixing may occur. The frequency of occurrence of billows in surface fronts, and a quantitative estimate of the mixing that they induce should be the subject of further research.

CHAPTER 5

Conclusions and proposals for further work

5.1 Summary

The aim of this thesis has been to identify and understand the location, characteristics and effects of Kelvin-Helmholtz (KH) billows in precipitating frontal zones. The main source of data used has been the high resolution Doppler radar at Chilbolton, which allows the radial component of the wind field to be measured in regions of precipitation. In addition, output from the Met. Office's Unified Model (UM) has been used together with the radar data to understand the factors responsible for the existence and properties of the billows that were observed.

5.1.1 The identification and occurrence of KH billows and shear layers

KH billows occur in stratified shear layers. Such layers may be found frequently in the atmosphere, especially in frontal zones where shearing of the wind with height may occur in approximate balance with the temperature structure across the front. In fact, when frontal zones are observed using shear RHIs, it is apparent that they frequently occur as very distinct multiple layers, with perhaps a tendency to be no more than around 1 km deep. This is very different from the way in which they are generally represented by present-day numerical weather prediction (NWP) models, in which the frontal zone will occur as a single stratified shear layer. The resolution of the mesoscale version of the UM in the lower and mid-troposphere (Fig. 4.2) is just sufficient to resolve the layers identified by the radar, so presumably their absence is due either to the inability of the model to represent the process which causes them, or the use of an excessively large horizontal diffusion (for computational reasons) which removes these layers, if they occur in a sloping frontal zone, as soon as they are formed.

Another notable feature of RHIs showing the radial component of the vertical shear in precipitating frontal regions is the ubiquity of cats-eye and braided structures which imply the presence of KH billows, and thus mixing, over depths which tend to be around 1 km (but no more). It does not appear, from an examination of the relevant literature, that RHIs of the vertical shear have been used before specifically to identify regions containing KH billows. The frequency of large-amplitude billows must therefore have been greatly underestimated in previous studies using Doppler radar, as it has been demonstrated that, unless the billows are also intense (i.e. having strong velocity perturbations associated with them), they may go completely undetected unless the vertical shear is displayed in addition to the original Doppler velocity. The method used is analogous to that used by Browning (1971) to estimate the frequency of KH billows occurring in the clear air during periods when strong wind shear existed. Studies have shown that energy dissipation by clear-air turbulence at high levels, itself partly caused by KH billows, may be of some significance for the larger scale circulation. It would now appear to be possible to include the effects of mixing within precipitating regions at lower levels in such a calculation, if an appropriate dataset were to be obtained.

5.1.2 The role of the mesoscale structure of a warm front in determining the location of billows

The case study forming the bulk of this thesis is based on radar observations made in the vicinity of a warm frontal zone. The kinematic and thermodynamic structure of the frontal zone was determined using a combination of Doppler radar data and mesoscale model output, showing that a sheared layer of air entering the frontal zone was lifted to saturation around 40 km north (ahead) of the surface front. This air came from behind and ahead of the surface front, and also from the boundary layer itself where the frontal zone intersected the ground. However, within the model these air-flows were kept separate as soon as they had left the boundary layer, as the model does not parameterise vertical mixing in the free atmosphere. The model's Richardson number, when calculated taking into account the saturation or otherwise of the air, shows a rather abrupt drop to substantially sub-critical values as soon the layer reached saturation. It is this abrupt change in Richardson number that is important, rather than the actual values which must inevitably have been subject to some error. Thus the onset of saturation allowed very low Richardson numbers to occur over a deep layer, whereas if saturation had not occurred, weak overturning would have prevented the Richardson number from becoming substantially sub-critical.

The very low Richardson number, in the presence of strong shear, had the effect of making the billows very intense, and thus easy to identify in the Doppler radar data. This is also consistent with measurements of their lifetime, which was around 50 minutes for each individual billow, as laboratory experiments by Thorpe (1973b) show that the time between the onset of small disturbances and the breakdown of the billow is inversely proportional to the initial Richardson number. It seems reasonable to suppose that most previous observations of billows in the clear air occurred over layers with only a moderately sub-critical Richardson number, as a very fast (i.e. with a time-scale less than a few minutes) process would be needed to create a very small Richardson number. Even so joint radar and aircraft measurements have shown that billows in the clear air may be associated with moderate and even strong clear-air turbulence (e.g. Browning *et al.* 1970b). Thus the billows described in this thesis may have been considerably more intense than most observed before in the clear air, as a direct result of the sudden onset of saturation. However, this may be partly offset by the fact that the magnitude of the shear in this case was not extremely large, and the scales responsible for turbulence encountered by aircraft are smaller than the primary billow scale.

5.1.3 Potential Shearing Instability

The processes responsible for the sudden decrease in Richardson number following saturation have led to the concepts of Potential and Conditional Shearing Instability (PSHI and CSHI, respectively). These are analogous to potential and conditional instability, terms which are frequently used to describe the static stability of the atmosphere. A layer exhibits CSHI if its bulk Richardson number is greater than 0.25 when calculated using (4.1) assuming the layer is dry and between 0 and 0.25 when calculated using (4.2) assuming the layer is saturated . For a layer to exhibit PSHI, any shear across the layer is assumed to be conserved during lifting, and the criterion for instability is that $0 < Ri < 0.25$ after lifting the layer to saturation. In practice, the assumption of conservation of shear across the layer may not be valid, especially if it takes some time to lift the layer to saturation. Other potential problems may occur from partial saturation of the layer, and limited extent of the layer upstream of the region of interest. The latter makes direct application of the idea of PSHI to the main case in this study difficult, although cases have been described where it would appear to be more appropriate (i.e. if saturation occurred further ahead of the surface front, or in flow over a mountain or ridge etc). Cases have also been identified where PSHI may be causing intense billows to occur in other frontal zones (e.g. Fig. 4.10), although these require further investigation.

5.1.4 Momentum flux calculations

The long duration of the observations has allowed measurements of mean wind velocity profiles both just upstream and downstream of the billows (a distance of around 40 km). These show an approximate doubling of the depth of the shear layer, although it is not obvious *a priori* whether this increase in shear layer depth is as a result of mixing by the billows, or some other process associated with the meso or synoptic-scale dynamics of the front. However, momentum flux calculations suggest that the billows may have been responsible for at least some of this change, although this conclusion is uncertain because of the restriction that only observations made directly perpendicular to the billows may be used in the analysis. Only a few such observations were available in the dataset available, leading to possibly large (but undetermined) errors in the analysis technique. The main significance of the calculation is that the method shows potential to be much more quantitatively useful if a dataset with appropriate scans were to be obtained in the future. Suggestions have been made for how the method could be validated and errors estimated, given such a dataset.

5.2 Future work

Billows of such intensity and amplitude as those described in this thesis do not occur along the whole length of every warm front, but it is not known how frequently they do occur. If, as seems likely, PSHI is necessary for them to occur *and* be intense over a large area and time, then it should be possible to forecast their occurrence by looking for suitable relative humidity and flow structures forecast by a mesoscale numerical weather prediction model. Accurate forecasting at least one day in advance of such events is important for planning the acquisition of such data, even if automated radar scanning sequences are to be used.

The following aspects need substantial observations in order to resolve some of the issues raised by this thesis (and other studies):

- The frequency of occurrence of KH billows in precipitating regions. An automated scanning sequence (perhaps similar to the FASTEX sequence shown on page 27, but traversing 360° in azimuth) could be used to obtain a "climatology" of KH billows in precipitating regions, perhaps concentrating on frontal regions.
- The manner of breakdown of KH billows in the atmosphere. If the billows break down on a scale one tenth that of the primary billows (i.e. no more than 500 m in the horizontal), this will be little more than the resolution of the radar as used here so it will not be possible to resolve the secondary instability. However, the resolution of 300 m is obtained by averaging over 4 gates each of length 75 m, in order to increase sensitivity. Given sufficient precipitation (probably more than existed in the relevant part of this study), the data from the individual gates could be used with either no averaging or averaging over fewer than 4 gates to give a range resolution between 75 and 300 m. It would therefore be possible, in principle, to resolve the processes responsible for the breakdown of the billows, although interpretation of the observations is unlikely to be straightforward.
- The effect of billows on the larger scale mean structure. The method used to calculate momentum fluxes could be used to obtain more reliable results, given sufficient scans perpendicular to the billows over the whole of their lifecycle. Also, more conventional methods could be used (e.g. Bryant and Browning 1975), if appropriate, to calculate the momentum fluxes. Ideally these would be obtained in conjunction with the high-resolution observations of the breakdown, as mentioned in the previous point.
- NWP models' representation of the effects of billows. Even though the mesoscale version

of the UM has sufficiently high vertical resolution, at least in the lower free troposphere, to resolve the effects of billows on mean profiles, it does not represent them, instead relying on an artificial horizontal diffusion applied for numerical reasons to remove sharp gradients. Work needs to be done to determine the problems associated with this approach (especially as the resolution of the model improves with successive versions of the UM), the role of KH billows in removing large gradients in the atmosphere, and the extent to which the effects of billows may or may not be represented as a purely diffusive process.

- Application of billow detection in the study of the role of mixing on atmospheric chemistry. Perhaps the most significant result presented in this thesis is the usefulness, even necessity, of using RHIs showing the vertical shear when trying to identify regions of mixing by KH billows. The simplicity of the method allows it to be used when collecting data in real time, thus aiding targeted observations of mixing in the atmosphere. This would be especially useful if joint radar/aircraft measurements were to be carried out. The chemical processes and consequences of mixing across frontal zones have yet to be studied in depth, and shear RHIs could provide a very useful tool for such studies.

References

Atlas, D., Metcalf, J. I., Richter, J. H., and Gossard, E. E. (1970). The birth of CAT and microscale turbulence. *J. Atmos. Sci.*, **27**, 903–913.

Batchelor, G. K. (1967). *An introduction to fluid mechanics*. Cambridge Univ. Press.

Blumen, W. (1984). An observational study of instability and turbulence in nighttime drainage winds. *Bound.-Layer Meteor.*, **28**, 245–269.

Bosart, L. F. and Garcia, O. (1974). Gradient Richardson profiles and changes within an intense mid-tropospheric baroclinic zone. *Quart. J. Roy. Meteor. Soc.*, **100**, 593–607.

Brown, W. O. J. and Rogers, R. R. (1997). Gravity wave and wind shear observations on the McGill weather and profiler radars. In *28th Conference on Radar Meteorology*, pages 512–513. Austin, TX, Amer. Meteor. Soc.

Browning, K. A. (1971). Structure of the atmosphere in the vicinity of large-amplitude Kelvin-Helmholtz billows. *Quart. J. Roy. Meteor. Soc.*, **97**, 283–299.

Browning, K. A. and Watkins, C. D. (1970). Observations of clear-air turbulence by high power radar. *Nature*, **227**, 260–263.

Browning, K. A., Harrold, T. W., and Starr, J. R. (1970a). Richardson number limited shear zones in the free atmosphere. *Quart. J. Roy. Meteor. Soc.*, **96**, 40–49.

Browning, K. A., Watkins, C. D., Starr, J. R., and McPherson, A. (1970b). Simultaneous measurements of clear-air turbulence at the tropopause by high-power radar. *Nature*, **228**, 1065–1067.

Browning, K. A., Hardman, M. E., Harrold, T. W., and Pardoe, C. W. (1973). The structure of rainbands within a mid-latitude depression. *Quart. J. Roy. Meteor. Soc.*, **99**, 215–231.

Browning, K. A., Bryant, G. W., Starr, J. R., and Axford, D. N. (1973a). Air motion within Kelvin-Helmholtz billows determined from simultaneous Doppler radar and aircraft measurements. *Quart. J. Roy. Meteor. Soc.*, **99**, 619–638.

Browning, K. A., Roberts, N. M., and Illingworth, A. J. (1997). Mesoscale analysis of the activation of a cold front during cyclogenesis. *Quart. J. Roy. Meteor. Soc.*, **123**, 2349–2375.

Bryant, G. W. and Browning, K. A. (1975). Multi-level measurements of turbulence over the sea during the passage of a frontal zone. *Quart. J. Roy. Meteor. Soc.*, **101**, 35–54.

Busak, B. and Brümmer, B. (1987). A case study of Kelvin-Helmholtz waves within an off-shore stable boundary layer: Observations and linear model. *Bound.-Layer Meteor.*, **44**, 105–135.

Chapman, D. and Browning, K. A. (1997). Radar observations of wind-shear splitting within evolving atmospheric Kelvin-Helmholtz billows. *Quart. J. Roy. Meteor. Soc.*, **123**, 1433–1439.

Chilson, P. B., Muschinski, A., and Schmidt, G. (1997). First observations of Kelvin-Helmholtz billows in an upper level jet stream using VHF frequency domain interferometry. *Radio Sci.*, **32**, 1149–1160.

Cullen, M. J. P. (1993). The unified forecast/climate model. *Met. Mag.*, **122**, 81–94.

Davis, P. A. and Peltier, W. R. (1976). Resonant parallel shear instability in the stably stratified planetary boundary layer. *J. Atmos. Sci.*, **33**, 1287–1300.

Davis, P. A. and Peltier, W. R. (1977). Effects of dissipation on parallel shear instability near the ground. *J. Atmos. Sci.*, **34**, 1868–1884.

Davis, P. A. and Peltier, W. R. (1979). Some characteristics of the Kelvin-Helmholtz and resonant overreflection modes of shear flow instability and of their interaction through vortex pairing. *J. Atmos. Sci.*, **36**, 2394–2412.

Doviak, R. J. and Zrnic, D. S. (1984). *Doppler radar and weather observations*. Academic Press.

Drazin, P. and Reid, W. (1981). *Hydrodynamic stability*. Cambridge University Press.

Drazin, P. G. (1958). The stability of a shear layer in an unbounded heterogeneous inviscid fluid. *J. Fluid Mech.*, **4**, 214–224.

Durran, D. and Klemp, J. (1982). On the effects of moisture on the Brunt-Väisälä frequency. *J. Atmos. Sci.*, **39**, 2152–2158.

Fritts, D. C., Palmer, T. L., Andreassen, Ø., and Lie, I. (1996a). Evolution and breakdown of Kelvin-Helmholtz billows in stratified compressible flows. Part I: Comparison of two- and three-dimensional flows. *J. Atmos. Sci.*, **53**, 3173–3191.

Fritts, D. C., Garten, J. F., and Andreassen, Ø. (1996b). Wave breaking and transition to turbulence in stratified shear flows. *J. Atmos. Sci.*, **53**, 1057–1085.

Gage, K. S. (1990). Chapter 28a: Radar observations of the free-atmosphere: Structure and dynamics. In *Radar in Meteorology*. D. Atlas, Ed., Amer. Meteor. Soc. 534–565.

Goddard, J. W. F., Eastment, J. D., and Thurai, M. (1994). The Chilbolton advanced meteorological radar: A tool for multidisciplinary research. *Electronics and Communications Engineering Journal*, **6**, 77–86.

Gossard, E. E. (1990). Chapter 27a: Radar research on the atmospheric boundary layer. In *Radar in Meteorology*. D. Atlas, Ed., Amer. Meteor. Soc. 477–527.

Hardy, K. R., Reed, R. J., and Mather, G. K. (1973). Observation of Kelvin Helmholtz billows and their meso-scale environment by radar, instrumented aircraft and a dense radiosonde network. *Quart. J. Roy. Meteor. Soc.*, **99**, 279–293.

Hazel, P. (1972). Numerical studies of the stability of inviscid stratified shear flows. *J. Fluid Mech.*, **51**, 39–61.

Hicks, J. J. and Angell, J. K. (1968). Radar observations of breaking gravitational waves in the visually clear atmosphere. *J. Appl. Meteor.*, **7**, 114–121.

Howard, L. N. (1961). Note on a paper of John W. Miles. *J. Fluid Mech.*, **10**, 509–512.

James, P. K. and Browning, K. A. (1981). An observational study of primary and secondary billows in the free atmosphere. *Quart. J. Roy. Meteor. Soc.*, **107**, 351–365.

Joly, A. *et al.* (1997). The fronts and Atlantic storm-track experiment (FASTEX): Scientific objectives and experimental design. *Bull. Amer. Met. Soc.*, **78**, 1917–1940.

Joss, J. and Waldvogel, A. (1970). A method to improve the accuracy of radar measured amounts of precipitation. In *14th Conference on Radar Meteorology*, pages 237–238. Amer. Meteor. Soc.

Keller, J. L. (1989). Clear air turbulence as a response to meso- and synoptic-scale dynamic processes. *Mon. Wea. Rev.*, **18**, 2228–2242.

Kennedy, P. J. and Shapiro, M. A. (1979). Further encounters with clear air turbulence in research aircraft. *J. Atmos. Sci.*, **37**, 986–993.

Klaasen, G. P. and Peltier, W. R. (1985a). The effect of the Prandtl number on the evolution and stability of Kelvin-Helmholtz billows. *Geophys. & Astrophys. Fluid Dyn.*, **32**, 23–60.

Klaasen, G. P. and Peltier, W. R. (1985b). The onset of turbulence in finite-amplitude Kelvin-Helmholtz billows. *J. Fluid Mech.*, **155**, 1–35.

Knox, J. A. (1997). Possible mechanisms of clear-air turbulence in strongly anticyclonic flows. *Mon. Wea. Rev.*, **125**, 1251–1259.

Koop, C. G. and Browand, F. K. (1979). Instability and turbulence in a stratified fluid with shear. *J. Fluid Mech.*, **93**, 135–179.

Lalas, D. P. and Einaudi, F. (1974). On the correct use of the wet adiabatic lapse rate in stability criteria of a saturated atmosphere. *J. Appl. Meteor.*, **13**, 318–324.

Lalas, D. P. and Einaudi, F. (1976). On the characteristics of gravity waves generated by atmospheric shear layers. *J. Atmos. Sci.*, **33**, 1248–1259.

Ludlam, F. H. (1967). Characteristics of billows clouds and their relation to clear air turbulence. *Quart. J. Roy. Meteor. Soc.*, **93**, 419–435.

Maslowe, S. A. (1973). Finite-amplitude Kelvin-Helmholtz billows. *Bound.-Layer Meteor.*, **5**, 43–52.

Merrill, J. T. (1977). Observational and theoretical study of shear instability in the airflow near the ground. *J. Atmos. Sci.*, **34**, 911–921.

Metcalf, J. I. and Atlas, D. (1973). Microscale ordered motions and atmospheric structure associated with thin echo layers in stably stratified zones. *Bound.-Layer Meteor.*, **4**, 7–35.

Metcalf, J. I., Stratmann, E., and Atlas, D. (1970). Ultra-High resolution radar structure of breaking waves and CAT. In *14th Conference on Radar Meteorology*, pages 83–88. Amer. Meteor. Soc.

Miles, J. W. (1961). On the stability of heterogeneous shear flows. *J. Fluid Mech.*, **10**, 496–508.

Miles, J. W. (1963). On the stability of heterogeneous shear flows, Part 2. *J. Fluid Mech.*, **16**, 209–227.

Muschinski, A. (1996). Possible effect of Kelvin-Helmholtz instability on VHF radar observations of the mean vertical wind. *J. Appl. Meteor.*, **35**, 2210–2217.

Nielsen, J. W. (1992). In situ observations of Kelvin-Helmholtz waves along a frontal inversion. *J. Atmos. Sci.*, **49**, 369–386.

Patnaik, P., Sherman, F. S., and Corcos, G. M. (1976). A numerical simulation of Kelvin-Helmholtz waves of finite amplitude. *J. Fluid Mech.*, **73**, 215–240.

Reiter, E. R., Lester, P. F., and Wooldridge, G. (1969). Spectral analysis of a breaking wave. *Clear Air Turbulence and its Detection,* Y.-H. Pao and A. Goldberg. Eds., Plenum Press, 21–33.

Roach, W. T. (1970). On the influence of synoptic development on the production of high level turbulence. *Quart. J. Roy. Meteor. Soc.*, **96**, 413–429.

Rosenhead, L. (1931). The formation of vortices from a surface of discontinuity. *Proc. Roy. Soc.*, **134**, 170–192.

Sato, T. and Woodman, R. F. (1982). Fine altitude resolution observations of stratospheric turbulent layers by the Arecibo 430 MHz radar. *J. Atmos. Sci.*, **39**, 2546–2552.

Scinocca, G. P. (1995). The mixing of mass and momentum by Kelvin-Helmholtz billows. *J. Atmos. Sci.*, **52**, 2509–2530.

Scotti, R. S. and Corcos, G. M. (1972). An experiment on the stability of small disturbances in a stratified free shear layer. *J. Fluid Mech.*, **52**, 499–528.

Starr, J. R. and Browning, K. A. (1972). Doppler radar measurements of clear air turbulence. In *15th Conference on Radar Meteorology*, pages 248–251. Amer. Meteor. Soc.

Stull, R. B. (1988). *An introduction to boundary layer meteorology*. Kluwer Academic Publishers.

Sykes, R. I. and Lewellen, W. S. (1982). A numerical study of breaking Kelvin-Helmholtz billows using a Reynolds-stress turbulence closure model. *J. Atmos. Sci.*, **39**, 1506–1520.

Takahashi, N., Uyeda, H., and Kikuchi, K. (1993). A Doppler radar observation on wave-like echoes generated in a strong vertical shear. *J. Meteor. Soc. Japan*, **71**, 357–365.

Thorpe, S. A. (1973a). Experiments on instability and turbulence in a stratified shear flow. *J. Fluid Mech.*, **61**, 731–751.

Thorpe, S. A. (1973b). Turbulence in stably stratified fluids: A review of laboratory experiments. *Bound.-Layer Meteor.*, **5**, 95–119.

Thorpe, S. A. (1985). Laboratory observations of secondary structures in Kelvin-Helmholtz billows and consequences for ocean mixing. *Geophys. Astrophys. Fluid Dyn.*, **34**, 175–199.

Thorpe, S. A. and Holt, J. T. (1995). The effects of laterally sloping upper and lower boundaries on waves and instability in stratified shear flows. *J. Fluid Mech.*, **286**, 49–65.

Trout, D. and Panofsky, H. A. (1969). Energy dissipation near the tropopause. *Tellus*, **3**, 355–358.

Turner, J. S. (1973). *Buoyancy effects in fluids*. Cambridge Univ. Press.

Wakimoto, R. M., Blier, W., and Liu, C. (1992). The frontal structure of an explosive oceanic cyclone: Airborne radar observations of ERICA IOP 4. *Mon. Wea. Rev.*, **120**, 1135–1155.

Wallace, J. M. and Hobbs, P. V. (1977). *Atmospheric Science*. Academic Press.

Wang, P.-Y., Parsons, D. B., and Hobbs, P. V. (1983). The mesoscale and microscale structure and organization of clouds and precipitation in midlatitude cyclones. VI: Wavelike rainbands associated with a cold-frontal zone. *J. Atmos. Sci.*, **40**, 543–558.

Weckworth, T. M. and Wakimoto, R. M. (1992). The initiation and organization of convective cells atop a cold-air outflow boundary. *Mon. Wea. Rev.*, **120**, 2169–2187.

Woods, J. D. and Wiley, R. L. (1972). Billow turbulence and ocean micro-structure. *Deep Sea Res.*, **19**, 87–121.

Xu, Q., Xue, M., and Droegemeier, K. (1996). Numerical simulations of density currents in sheared environments within a vertically confined channel. *J. Atmos. Sci.*, **53**, 770–786.

Young, K. C. (1993). *Microphysical processes in clouds*. Oxford University Press.